Development of an Active Aeroelastic Continuous Trailing Edge Wind Tunnel Wing Model for Drag and Gust Load Minimization

Tyler Mundt

A thesis

submitted in partial fulfillment of the

requirements for the degree of

Master of Science in Aeronautics & Astronautics

University of Washington

2019

Reading Committee:

Eli Livne, Chair

Carl Knowlen

Program Authorized to Offer Degree:

William E Boeing Department of Aeronautics & Astronautics

University of Washington

Abstract

Development of an Active Aeroelastic Continuous Trailing Edge Wind Tunnel Wing Model for Drag and Gust Load Minimization

Tyler Mundt

Chair of the Supervisory Committee:
Professor Eli Livne
William E Boeing Department of Aeronautics & Astronautics

An actively controlled, aeroelastically-scaled wind tunnel wing model was developed for low-speed tests of real-time drag and gust load alleviation by wing shaping for the SSCI-DIRECT project. The model uses eight independently controlled trailing edge flaps, and contains accelerometers and strain gauges for load sensing. The design builds off three VCCTEF aeroelastic models: two with manual adjustment and one with active control. A detailed NASTRAN model was developed and validated by both static load and modal tests. Wind tunnel testing is currently underway at the University of Washington's Kirsten Wind Tunnel.

TABLE OF CONTENTS

LIST OF FIGURES

LIST OF TABLES

ACKNOWLEDGEMENTS

This project would not have been possible without the support of Dr. Nhan Nguyen and his team from NASA Ames, Dr. Jovan Boskovic and his team at Scientific Systems Company, Inc. (SSCI), and Prof. Eli Livne's Boeing Endowed Aeronautics and Astronautics Professorship. From these teams, a special thanks to Benjamin Krosner of SSCI for his work on the initial wiring schematics and Arduino code, and Dr. Nicholas Cramer of NASA Ames for his work designing the double-jointed flaps and reviewing structural and mechanical design. Thanks to Dr. Marat Mor for his expertise and efforts in creating the NASTRAN model. Thanks also to Antonio Deleo for his guidance and assistance in the skin, assembly, and patching layups. In addition, thanks to Eliot George at the University of Washington William E. Boeing Department of Aeronautics and Astronautics for his assistance in flexible transition strip design and sourcing, as well as electrical troubleshooting. From the Kirsten Wind Tunnel, thanks to Dr. Carl Knowlen, Matt Hudgins, and the student crew for their assistance in manufacture and testing. Also, thanks to Nathan Precup for his work on, and guidance from, Wing III. Finally, thanks to Aidan Conrad and all the other graduate students who helped with the assembly layup and wiring.

1. INTRODUCTION

From the early days of aviation, the capacity of flying machines to change their shape during flight in order to perform and handle optimally at different flight conditions has been a key element of their design and operation. High-lift systems in the form of trailing edge (TE) and leading edge (LE) flaps have been used to adapt an aerodynamic shape optimized for a specific mission performance to the requirements of take-off, landing, and approach. The utilization of LE and TE flaps, via flight condition dependent scheduling, has been used for years for performance enhancement, maneuver load control, gust load alleviation, and ride comfort [1]-[4].

The small number of control surfaces available for wing shaping and active control during flight has limited this corresponding design space. Moreover, the spanwise breaks and sharp edges between conventional control surfaces lead to increased drag and noise when activated. Inspired by the way birds and insect change their shape during flight, aeronautics research has struggled for years to develop efficient "morphing" configurations: configurations that would change shape in-flight in a smooth way, both in terms of time and final geometry.

Advances in this area in the 1980s included the AFTI-F111 Mission Adaptive Wing (MAW) project [5]-[9], with more recent work in this area reported in reference [10]. Developments over approximately the last twenty years in structural optimization, materials, and actuation technology have led to further developments, such as the adaptive compliant trailing edge [11]-[12]. A survey of recent developments in aircraft morphing technology can be found in reference [13], and in books such as references [14]-[17].

The Variable Camber Continuous Trailing Edge Flap (VCCTEF) wing concept emerged from collaboration between NASA and Boeing [18]-[19]. The core idea was to take advantage of developments in actuation and control technology to construct wing trailing edges made of a numerous small, independently-controlled segments connected to each another by flexible viscoelastic strips. This resulted in smooth, deformed shapes of the TE without gaps. The concept is shown in Figure 1. A portion of the substantial work accomplished on the various aspects of this technology is covered in references [18]-[33].

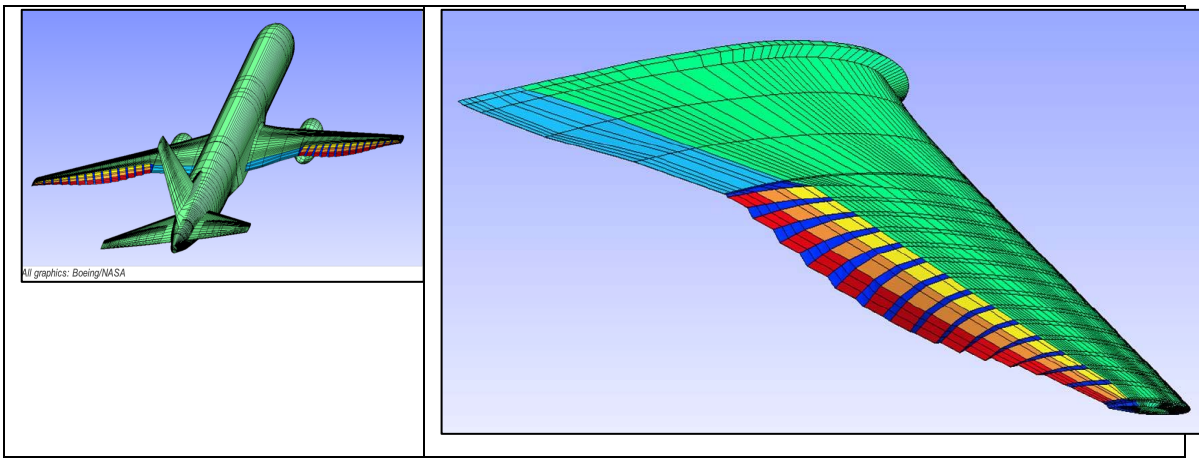

Figure 1: The VCCTEF concept (graphics courtesy Boeing / NASA)

To provide experimental data, two aeroelastically-scaled wind tunnel models were developed and tested at the University of Washington. First was a model of the General Transport Model (GTM, similar to a Boeing 757, but with a more flexible structure) in the clean configuration. This was followed by a GTM in the high-lift configuration with LE slats and a Fowler flap. These two models are denoted as Wing I and Wing II, respectively. Wing I and Wing II are described in references [31]-[33], and are shown in Figure 2 and Figure 3.

Figure 2: The aeroelastically-scaled GTM wing in the clean configuration at University of Washington's Kirsten Wind Tunnel

Figure 3: The aeroelastically-scaled GTM wing in high-lift configuration at University of Washington's Kirsten Wind Tunnel

These two models were tested at low speeds, with the TE segments moved manually from one test run to another. Drag, lift, and moment data was gathered together with aeroelastic deformation information through a Vicon optical system.

After completion of these tests, the view shifted to the pursuit of an actively controlled Wing III. Here, active control indicated a slow, quasi-steady response, where control surfaces would be slowly deflected by their individual actuators in order to optimize the shape of the wing for minimum drag over lift (subject to constraints on the absolute and relative control surface motions and measured loads). This system was to operate directly with wind tunnel lift and drag measurements, then adjust its shape to changes in-flight conditions based on pre-tested, pre-programmed control law scheduling synthesis. The ultimate vision here was for an airplane to change its shape in-flight to the current optimal configuration in response to measured fuel flow, internal loads, and flap segment motion constraints [34]-[37].

With the launch of the Wing III development, a decision was made to shift from the GTM geometry to the Common Research Model (CRM) geometry. The CRM was developed as a public domain airplane geometry representative of advanced passenger jets, to be used by CFD developers internationally [38]-[39]. The development of Wing III is described in references [40] and [42]. Results of tests at the University of Washington's Kirsten Wind Tunnel with the Wing III model are described in reference [41]. CAD definitions of the Wing III model are shown in Figure 4 – Figure 6. Of note in Wing III was the housing of all actuation system components inside the outer mold line (OML) of the clean wing.

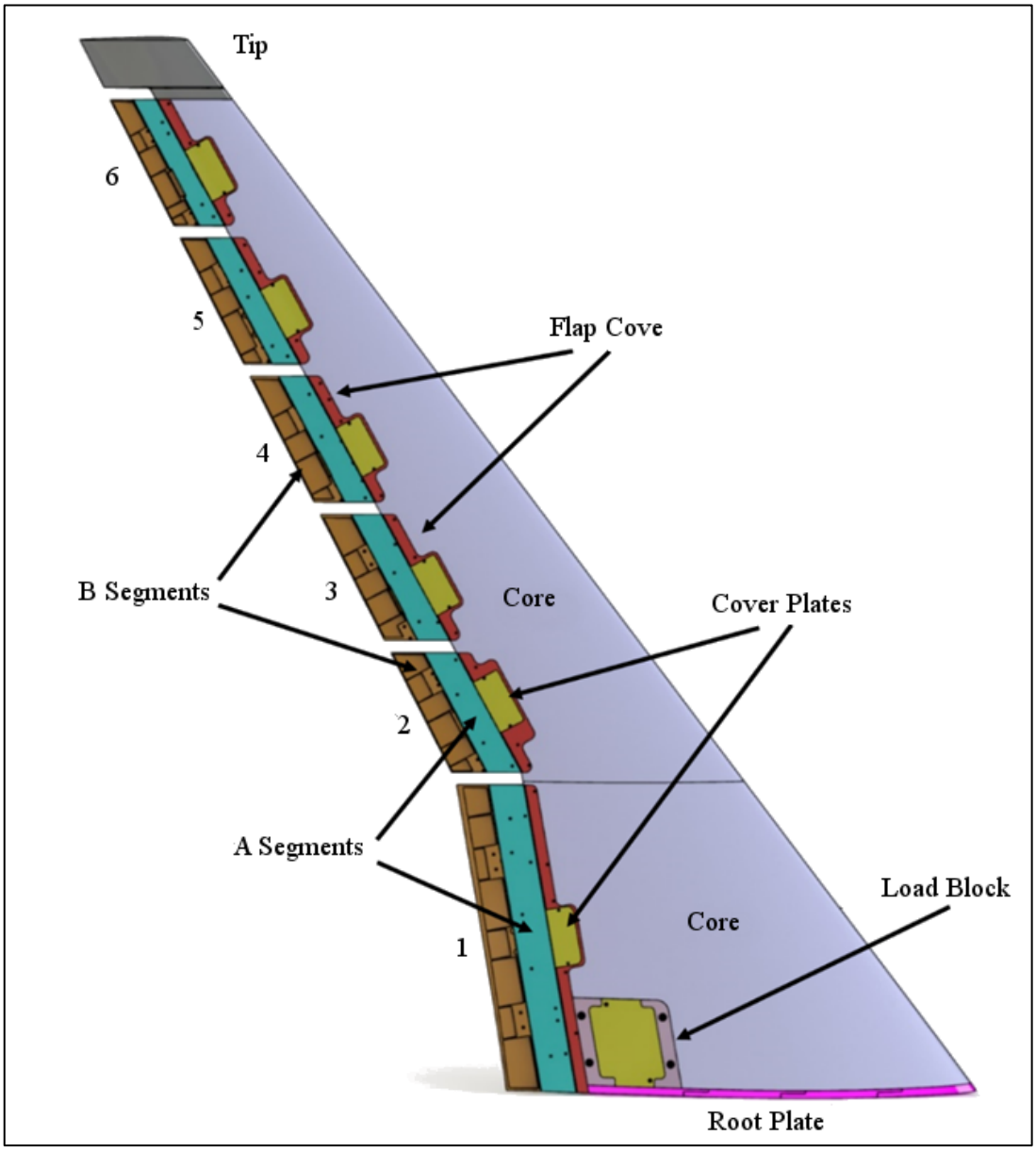

Figure 4: The CRM-based UW Wing III model layout

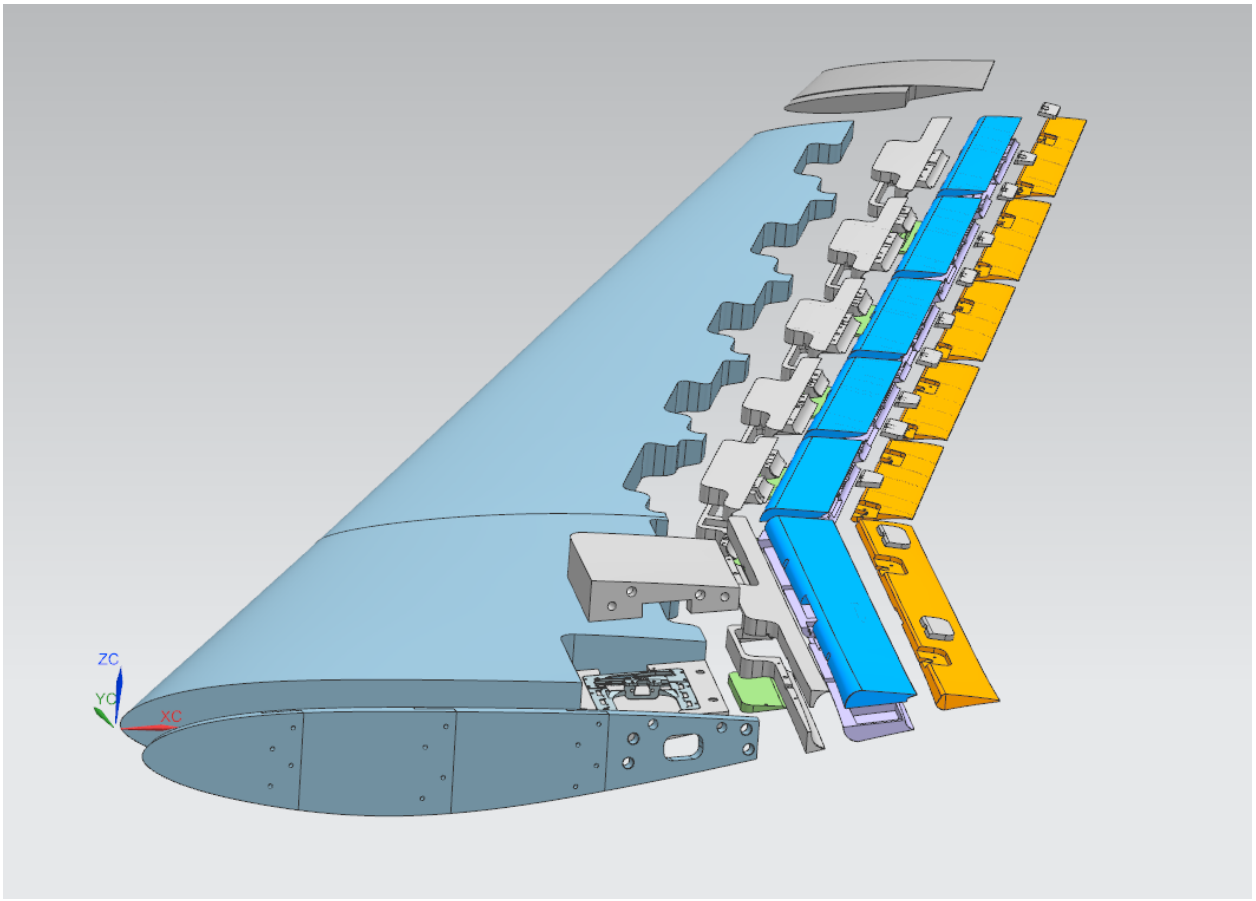

Figure 5: Construction of the Wing III aeroelastic model

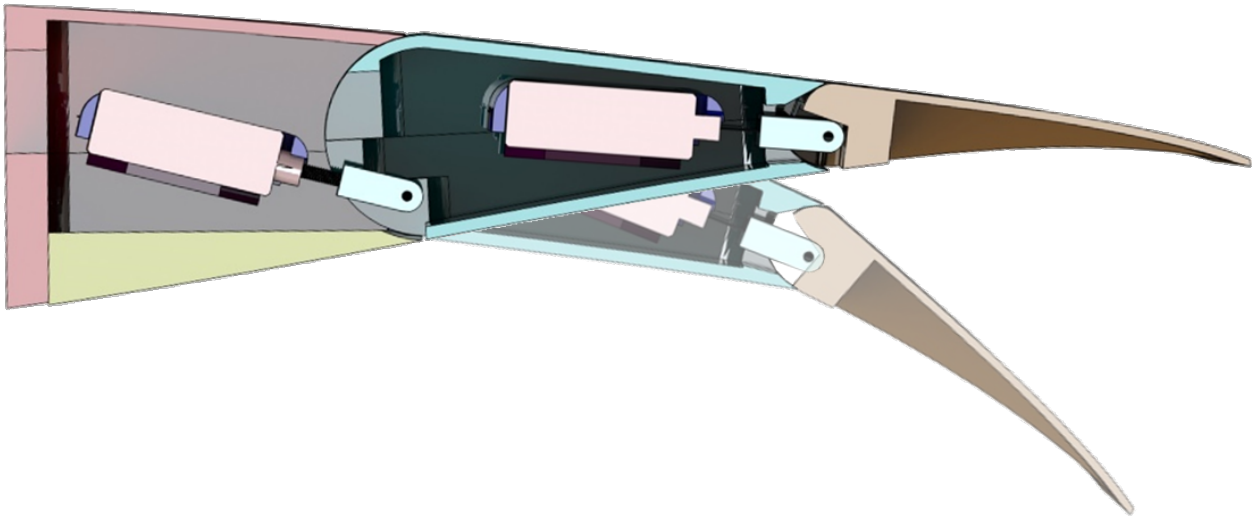

Figure 6: Actuation side cutaway view of Wing III

2. WING IV MOTIVATION AND GOALS

While leading to useful test results, the Wing III aeroelastic model did not perform as well as hoped. The primary deficiencies included actuation strength and accuracy, as well as some structural issues. The automated shape optimization process, based on the wing communicating with the wind tunnel's balance, had to be done in steps with shape changes obtained by a mix of manual and automated operation.

The drive screw connecting the modified wing servo and the driven bar often buckled or pulled out of the servo (as it was fastened using two-part structural epoxy). Alignment was also an issue during assembly as the drive screw was mounted by hand. In addition, even with the worm gear style drive, the servos themselves often overloaded. These issues lead to frequent repairs, including an entire replacement of the wire bundle when a power supply overloaded. Component accessibility, especially the wire bundle itself, compounded this issue, as the replacement of a single component was often on the time scale of an hour. The location of these actuation components of Wing III can be seen in the cutaway in Figure 7.

The position sensing of the actuation system was accomplished with incremental linear encoders. Their strips often buckled or became caught on surrounding parts. Also, this position sensing took place after the driven bar, rather than at the actual rotation hinge, and was thus unable to see, let alone correct, motions of the flap allowed by mechanical slop. Overall, these issues led to significant hysteresis, and prevented the flaps from automatically achieving consistent positions for the same command. The

usage of an incremental rather than absolute position sensing system also made this issue worse, as the index was often missed on the strip.

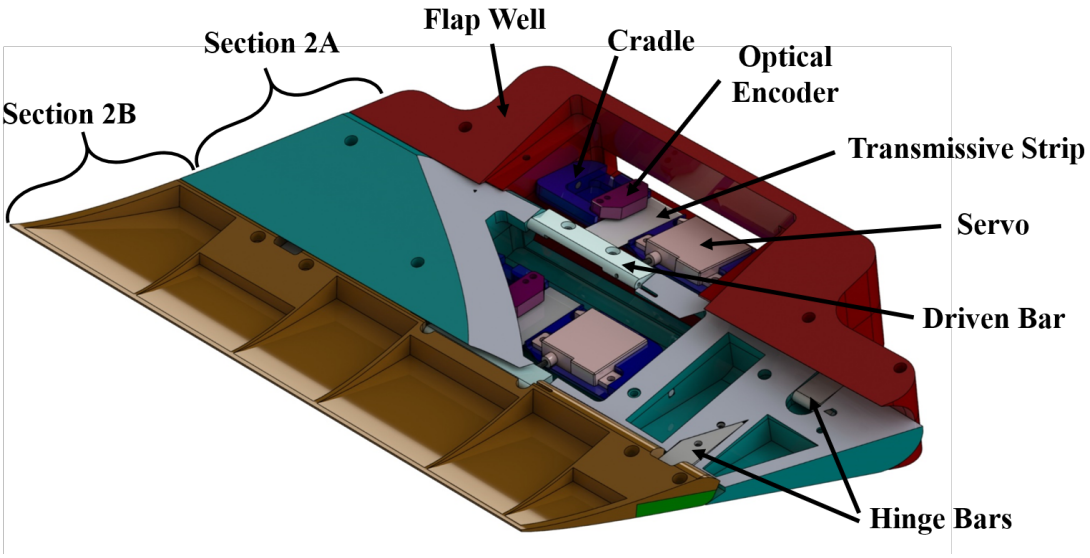

Figure 7: Labeled cutaway of Wing III double-jointed actuation

Structurally, Wing III experienced debonding of the fiberglass skin along its trailing edge on both the upper and lower surface, primarily along the aluminum flap wells. This was often corrected with epoxy, but was never permanent. Based on wind tunnel data, it was also suspected there was creep in the internal polystyrene foam as there was a consistent discrepancy in clean wing test curves between the morning, after the wing was mounted unsupported through the evening, and at the end of a day of testing. Finally, the Vicon deformation data showed the large rigid aluminum flap wells prevented the wing from deforming in a continuous manner, leaving only a small portion of the total span (between wells) to provide deformation.

After completing the drag reduction tests with Wing III, the focus of testing shifted to include gust load alleviation (GLA). This would require faster actuators, with a frequency bandwidth that allowed control of the first bending mode. In addition, this

would require load-sensing capabilities (in the form of accelerometers and strain gauges) to be mounted to the wing. These new requirements, along with the outstanding issues described in Wing III, motivated the development of a new test model: Wing IV.

The goal of Wing IV was to develop an actively controlled, flexible wing capable of simultaneously shaping itself for drag optimization while reducing encountered gust loads. Lessons from the previous three wings were used to guide the design and set requirements.

A central goal of Wing IV was to have a first bending frequency within the range of the selected actuators. An early review of available actuators placed this requirement, for both the structure and actuators, to be in the 2-2.5 Hz range (Wing III as-built was 2.8 Hz). While maintaining frequency response, the actuators also had to handle the maximum foreseeable load. The requirement to keep all actuators within the OML was removed as a requirement to accomplish this. Position feedback also needed to be revamped, taking into account mechanical slop, while also providing repeatable results. In addition to the lower first bending frequency requirement, the wing's structure had to maintain or improve the flexibility of Wing III, while preserving strength and bonding through the expected operational range (10 psf, up to a C_L of 1) and gust loads. Furthermore, this strength had to be maintained while achieving better accessibility to internal components. Finally, Wing IV had to include load sensing in order to read, and then respond to, an incoming gust.

3. MODEL DESIGN

The OML and overall geometry of Wing IV are identical to Wing III, and used the same molds during manufacture. The development of the Wing III CRM OML and the corresponding molds is described in Chapter 2 of reference [42]. The overall dimensions of these wings are shown in Table 1.

Table 1: Wing III and IV Geometry

Span	85 inches
Yehudi Break	25 inches
Root Chord	38.1 inches
Yehudi Chord	23.25 inches
Tip Chord	8.8 inches
Wing Area	12 sq. ft.
LE Sweep	37 degrees

The flap layout of Wing IV used the same number of bays (six) as the previous wing, but has a reduced number of total flaps. Wing IV used eight control surfaces, shown with their naming conventions in Figure 8. Flap 5B and 6B were dropped from Wing III in order to provide more control authority to these GLA-focused flaps, while also reducing the number of protrusions from actuators at the relatively thin bays near the tip. Flap 3B and 4B were dropped due to time constraints (speeding up design and manufacturing time in order to meet test deadlines). These two flaps could still be designed and installed at a later date, as the actuator and flap mounts were still implemented into the built model.

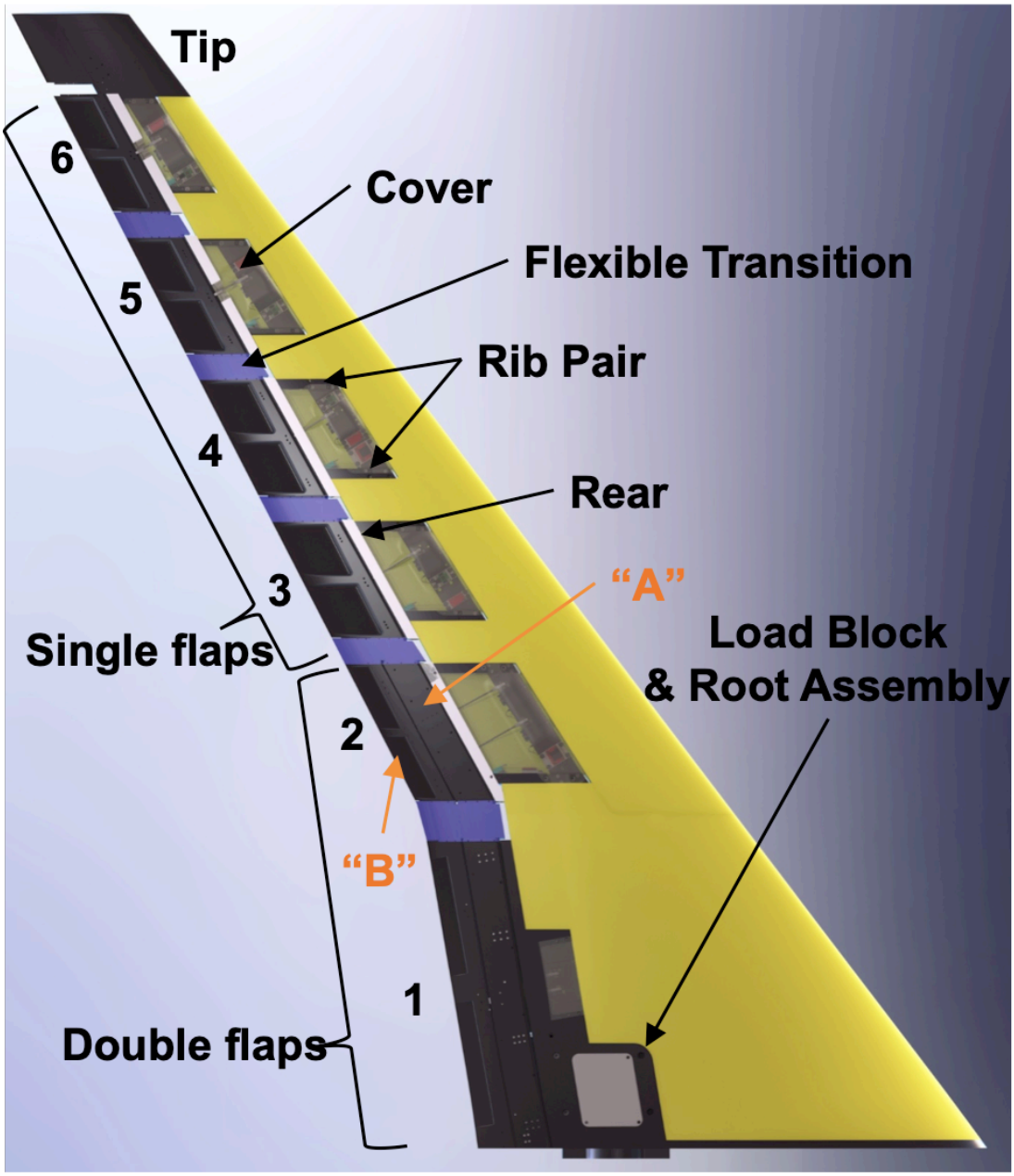

Figure 8: Labeled bottom view of Wing IV CAD Model

4. STRUCTURAL DESIGN

A notable deviation from Wing III was the addition of internal structural components beyond the flap wells along the TE, which were removed. A spar runs nearly the entire span of the wing, and has actuators and sensors mounted to it. Two ribs run from the spar in order to mount each flap. A cover, which allows accessibility to the spar-mounted components, as well as the wire bundle, was mounted to each rib pair. C-shaped rears complete the trailing edge OML. The root assembly and tip also received a redesign.

The spar was made from aluminum 6061-T6, and closely followed the elastic axis to minimize the effect on stiffness. The primary motivations for the spar were to provide an internal mounting surface for the load sensing system, and to have more room within the wing to mount larger actuators (placing them closer to the thickest portions of the wing). For the latter purpose, the spar is angled a few degrees upward from the predicted elastic axis to maximize mounting volume. The spar sweep is shallower than the LE at 32.15 degrees, and the upward angle from a plane perpendicular to the root is 5.49 degrees. The rectangular spar was 94 inches long, 2 inches wide, and 0.1285 inches thick. A cutaway view of the spar as seen from the TE can be seen in Figure 9, and a view of the spar placement from the lower surface with the lower foam pieces and covers removed can be seen in Figure 10. The spar mounts to the root plates using two custom L-shaped brackets, which can be seen in Figure 11.

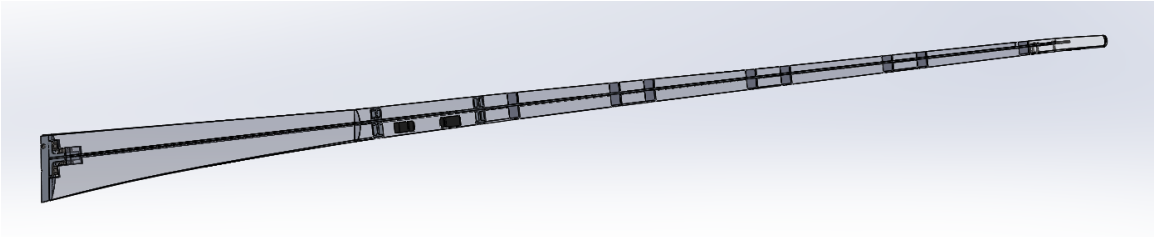

Figure 9: TE cutaway view of spar and rib placement in OML

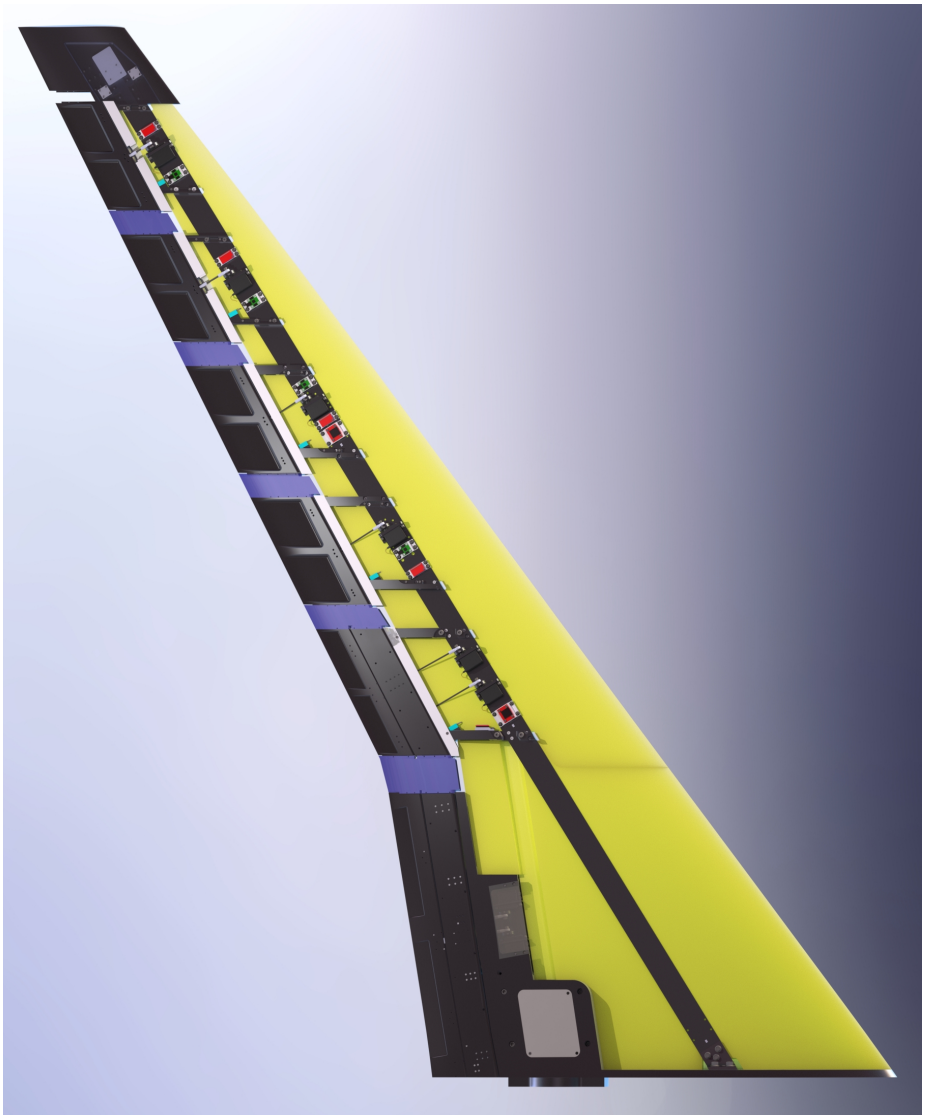

Figure 10: Bottom view of internal structure with foam and covers removed

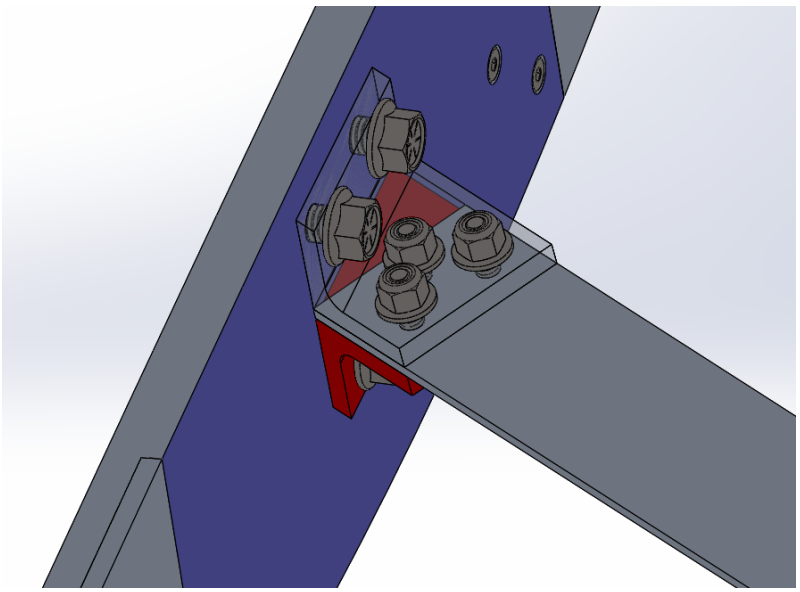

Figure 11: Spar L-bracket attachment

A pair of ribs attaches to the spar in order to mount the flaps for Bays 2 - 6. Each is mounted perpendicular to the spar and along a chord line parallel to the root. For Bays 2 - 4, the ribs are shaped similar to I beams to reduce weight and provide a mounting surface for rivets should debonding become an issue. The thickness of the OML towards the tip did not allow this in the Bay 5 and 6. The ribs do not extend towards the LE beyond the spar, and follow the OML on the upper and lower surfaces. The ribs also provide threaded mounts for weights, mounting for the access covers, mounting for the string potentiometers for actuation, and a pass-through at the spar for wiring. Table 2 describes the size and location of the ribs, and Figure 12 shows the ribs attached to the spar during assembly. The spar distance in Table 2 indicates the distance along the spar's LE from the root plate to the surface of the rib that faces the root.

Table 2: Rib Sizing and Positions

Rib	Width	Chord Length	Spar Distance
2 Inner	0.75 in	6.75 in	31.49 in
2 Outer	0.75 in	6.03 in	41.28 in
3 Inner	0.75 in	5.72 in	45.91 in
3 Outer	0.75 in	5.20 in	53.86 in
4 Inner	0.75 in	4.90 in	58.49 in
4 Outer	0.75 in	4.38 in	66.45 in
5 Inner	0.5 in	4.06 in	71.22 in
5 Outer	0.5 in	3.52 in	79.18 in
6 Inner	0.5 in	3.20 in	83.81 in
6 Outer	0.5 in	2.65 in	91.76 in

Figure 12: Ribs and rears mounted to spar during assembly

The flaps are smaller spanwise from Wing III by one inch in order to increase the width of the flexible transition strips. This was done to reduce the load on the actuators should large relative flap deflections be experienced, and avoid tearing of the strips themselves in such a scenario. For Bays 2-6, the flaps extend 0.23 inches from the outer rib towards the tip, and 1.5 inches from the inner rib towards the root, as measured along the spar. Flap 1 extends 23.6 inches from the root plane.

C-shaped rears fill out the OML in the interface between the flaps and ribs. These rears are mounted to both ribs, and match the width of the flaps. The C-profile, much like the I-shape on the ribs, was intended to provide a mounting surface for rivets should skin debonding become an issue. Those on Bays 5 and 6 had cutouts and reinforcement to allow clearance for the actuation control rods. All five rears were originally 3D printed using stereolithography from Accura Xtreme White 200. After collapses from vacuum bag forces during the assembly layup, described in Chapter 5, Bays 2- 4 were reprinted with vertical support pylons. Bays 3 and 4 were also reprinted out of Somos 9120, a more flexible material. Bay 2 was also reprinted (still in Accura Xtreme White 200) to have small, removable winglets on the bottom surface to provide wrench clearance for the mounting of Flap 2.

Between each pair of ribs a plastic cover was placed to allow easy accessibility for repairs, and provide an aerodynamic fairing for actuator protrusions. The covers followed the bottom OML, spanned the gap between the ribs, and ran from the LE of the ribs to the C-shaped rears. Covers for Bays 5 and 6 also went over a cutout in the center of their respective rears to cover the actuation linkage. Covers for Bays 2, 5, and 6 were made from Accura Xtreme White 200, and Bays 3 and 4 were made from Somos 9120. A CAD figure of Bay 4, showing the I-shaped ribs, the C-shaped rear (white), cover (transparent gray), and flap mounting is shown in Figure 13. A completed Bay 2 mounted to a mock spar can be seen in Figure 14.

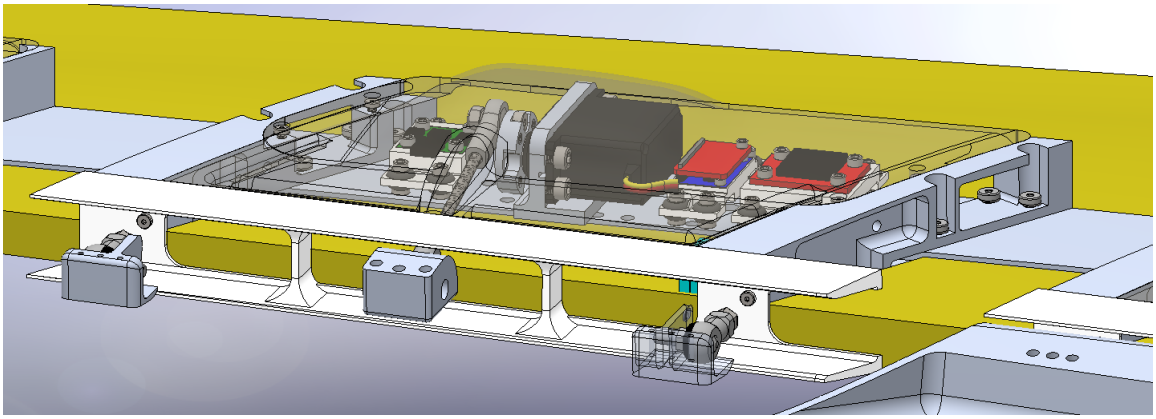

Figure 13: CAD view of Bay 4 with flap removed

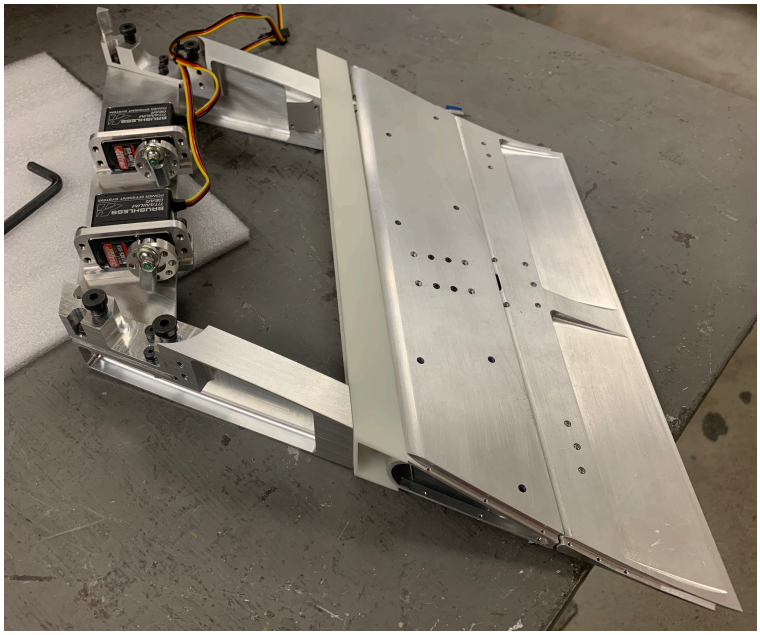

Figure 14: Completed Bay 2 with flap mounted

The root assembly also received an update over Wing III. The entire assembly, like the rest of the metal structure, was made from aluminum 6061-T6. The number of root plates was reduced from four to three to ease placement of the spar mounts. The adapter to the sidewall balance was also altered by -2.24 degrees to correct an offset from the sidewall's zero angle of attack seen in Wing III CAD and testing. The load block was also enlarged to allow the mounting of a larger board inside (an Arduino Due rather than

a Pro Mini), while maintaining clearance for the wire bundle. The flap well for Bay 1 remained in the design, but experienced two major alterations: adjustment of the cavities to match the new actuators and flap mounting, and the addition of physical mounting to the rest of the root assembly through four 1/4-20 screws. A CAD view of the root assembly without the neighboring foam can be seen in Figure 15.

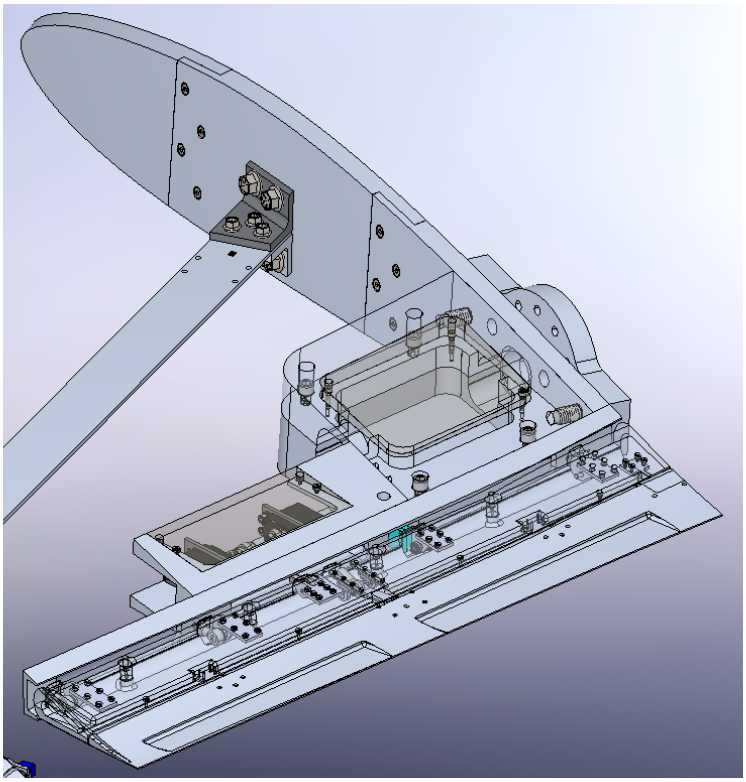

Figure 15: Root metal assembly CAD

The tip in Wing III was 3D printed and bonded to the foam. The tip for Wing IV, in order to make it heavier to lower the first bending frequency, was made from aluminum 6061-T6 and mounted to the end of the spar. It was made out of two pieces. The core piece held two accelerometers, attached to the spar, provided a pass-through for wires, and had a cavity for mounting additional weight. The second piece mounted to the core and completed the OML. During testing, a 4140 alloy steel block was used for the

weight, which brought the total mass at the tip to 3.58 pounds. An image of the tip core with the weight and two accelerometers mounted can be seen in Figure 16.

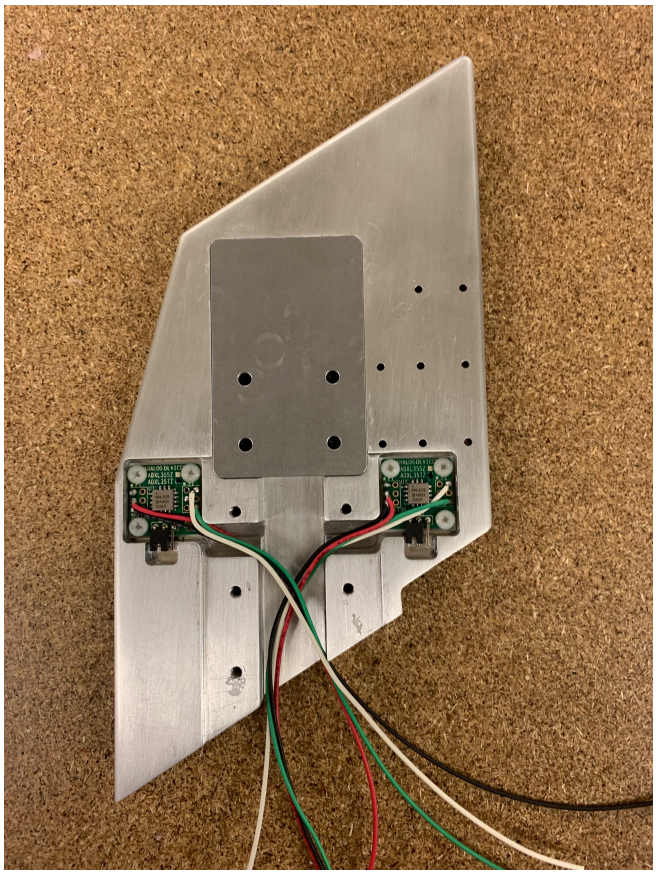

Figure 16: Tip core with mounted accelerometers and weight

The skins were made using the same fiberglass, fiber orientation, and molds as Wing III. The skin was four plies of 1.43 oz/yd^2 Orca Composites style OC003 plain weave fiberglass (comparable to style 108), and was cured with EpiKote 135 resin. Fibers were laid in alternating layers at +/- 45 degrees to the elastic axis.

Prior to skin manufacture, six test coupons were made for both 3- and 4-ply versions of the skin. From tensile Instron testing, the average 3-ply coupon had an elastic modulus of 1.04E6 psi and an ultimate tensile strength of 7,400 psi. For the 4-ply, the elastic modulus was 1.24E6 psi and the ultimate tensile strength of 13,000 psi. While the

3-ply would have been more flexible, preliminary models indicated it would be too weak for the intended range of operation.

To combat the polystyrene foam creep in Wing III, rigid polyurethane foam was selected instead. The four pounds per cubic foot Last-A-Foam FR-3700 was used. Wing III used two pieces of foam, split spanwise at the Yehudi break. To account for the spar, these pieces were then split along the spar, and voids were added for the ribs, wire bundle, and actuation mounting. To provide more resilience to the stress concentration seen at the trailing edge of the Yehudi break on both Wing III and the subscale wing, these pieces also overlapped across the Yehudi break. An exploded view of the foam from an early version of the CAD model is shown in Figure 17.

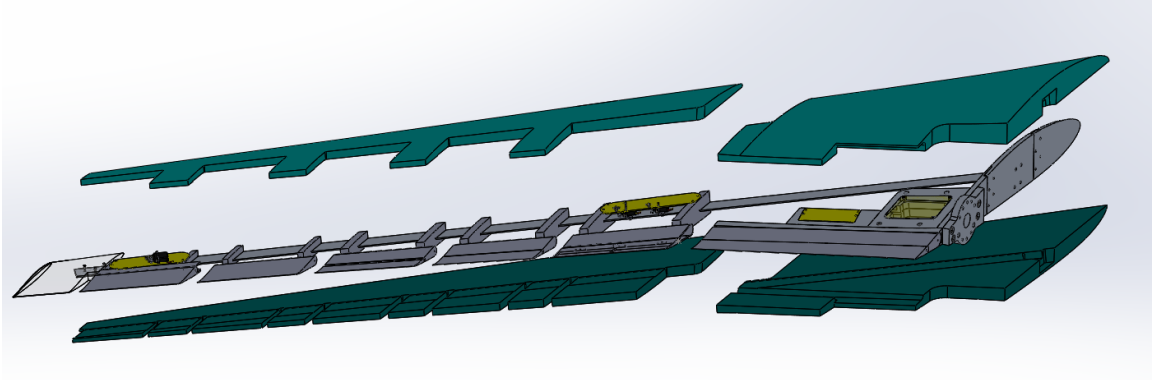

Figure 17: Bottom view of exploded foam assembly in early CAD model

The original flexible transition strips for Wing III had aluminum sidewalls and Mold Max 20 RTC silicone mold rubber as the flexible web. These were too stiff, constricting actuator movement and preventing a smooth spline at the TE. Eliot George, a University of Washington Aeronautics and Astronautics Engineer, designed a replacement set for Wing III that used dual-material 3D printing. A similar set was designed for Wing IV to match the new flap geometry, and used updated materials. These were printed as single parts by FATHOM in Seattle, WA using a polyjet printer. The

sidewalls were made from Stratasys Digital ABS Plus, and the flexible filler was Stratasys Agilus30. An image of the three transition strips for Wing III and IV is shown in Figure 18, and an installed strip in Wing IV can be seen in Figure 19.

Figure 18: Original Wing III (left, pink), 3D printed Wing III (middle, black), and 3D printed Wing IV (right, white) flexible transition strips

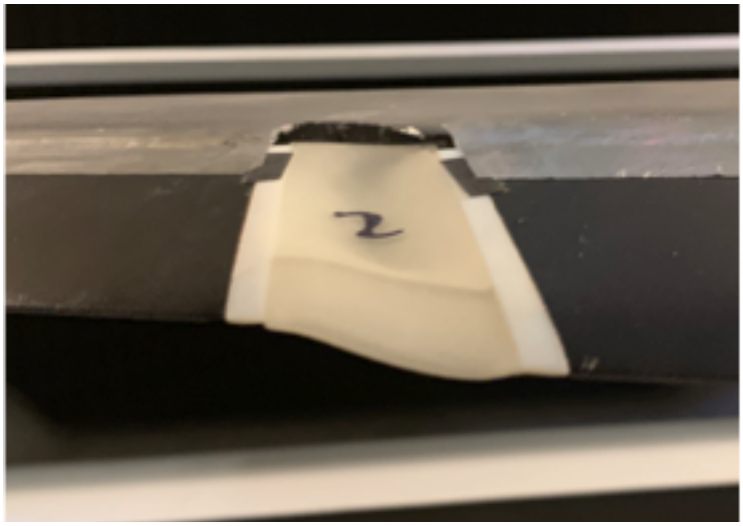

Figure 19: Wing IV installed dual material transition strip

5. WING CONSTRUCTION

The fiberglass skins were cured individually in their respective molds at room temperature under vacuum using a wet layup. An image of the two skins curing in their molds can be seen in Figure 20. Prior to the assembly layup, the entire internal metal assembly, including the spar, root, ribs, and rears, was assembled. Any fastener not secured with a nylon-insert locknut was secured using Loctite 262. The completed metal assembly can be seen in Figure 21.

Figure 20: Upper and lower skins curing under vacuum in their respective molds

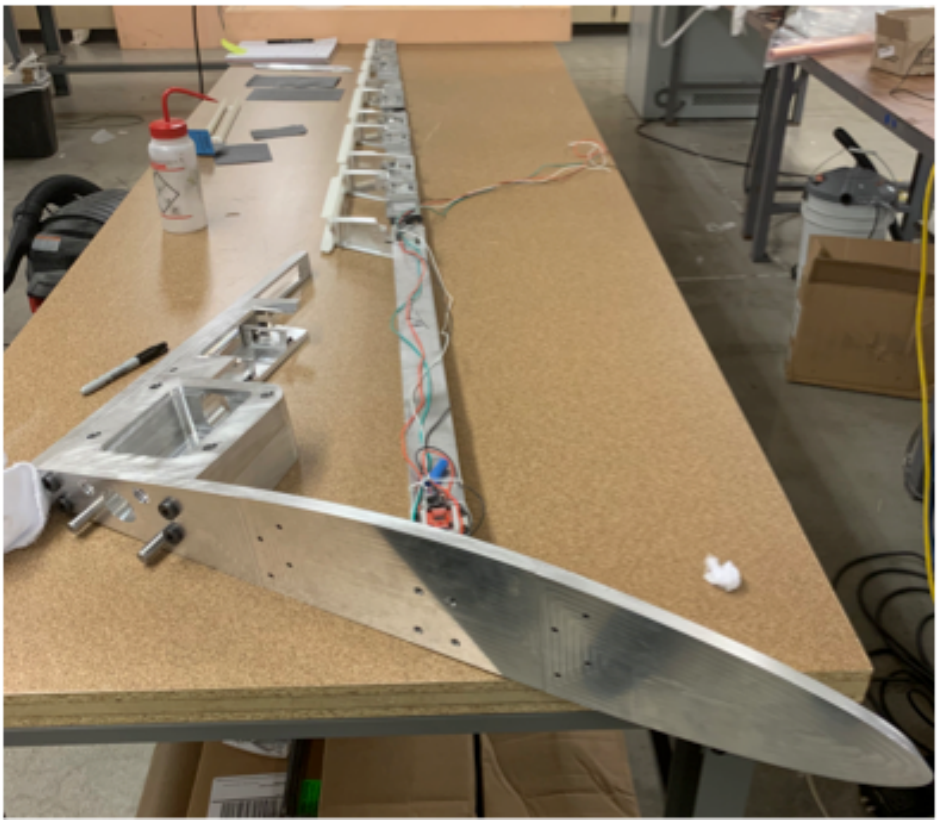

Figure 21: Complete internal metal assembly prior to install

To assemble the wing, the upper skin was laid in its mold and coated on the inner surface with Loctite E-120HP structural epoxy. The upper foam, followed by the metal assembly, and finally the lower foam was laid on top, with epoxy applied on both sides of contacting surfaces. A hand-cut carbon fiber section was then placed around each opening on Bays 2-6 along the ribs, rears, and foam on the bottom surface to provide reinforcement for the planned holes for the covers. These used the same Epikote 135 resin for curing. After this, the bottom skin was laid on top of the assembly. Finally, the full assembly was placed under vacuum and allowed to cure for two days. This total process was called the assembly layup, and intermediate pictures taken during this layup can be seen in Figure 22 and Figure 23.

Figure 22: Wing IV in the middle of assembly layup

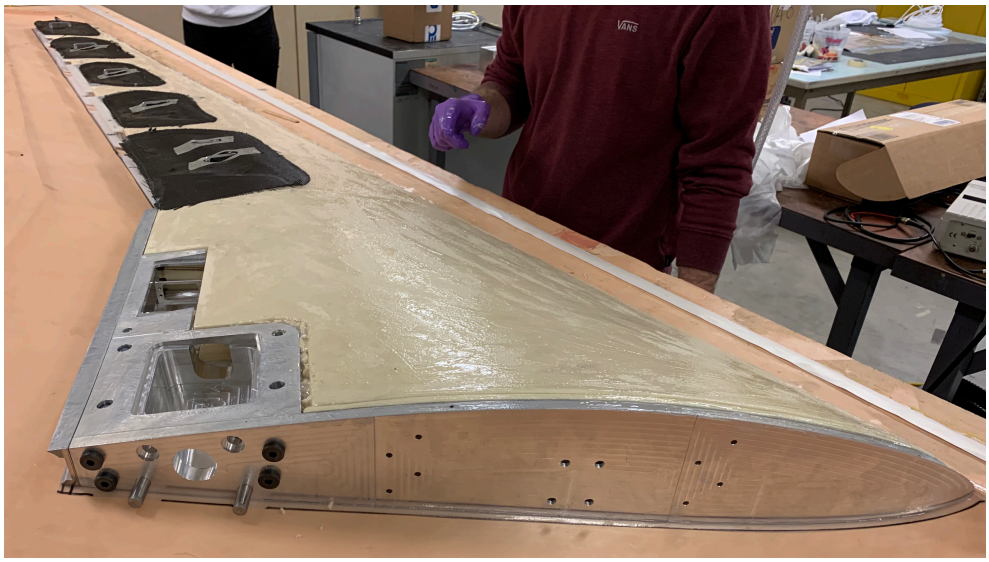

Figure 23: Wing IV prior to bottom skin (note carbon fiber reinforcement Bays 2-6)

Overall, the assembly layup was successful, but unsupported sections led to damage from the vacuum loads on the bottom surface. The plastic rears lacked vertical supports on Bays 2-4, which led to collapses. Furthermore, since the skin was so thin, it could not support itself over the empty gaps between ribs where actuation would be mounted on Bays 2-6. On Bays 2, 4, and 5, this led to the formation of cracks that propagated towards the LE beyond the cuts planned for the access covers. Finally, at the root, a piece of foam thinned to provide a pass-through for the wire bundle also collapsed, which led to cracks and wrinkles over most of the root assembly. A collage of these failures can be seen in Figure 24.

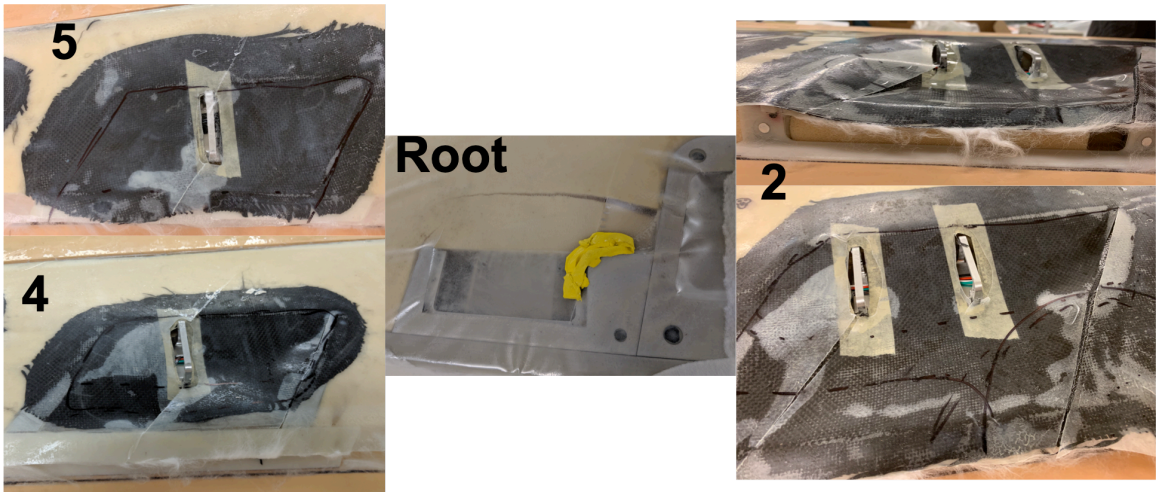

Figure 24: Skin cracks and failures after assembly layup

To prevent crack propagation and further damage to the wing, smoothly cut sections of the skin were removed, with at least an extra quarter of an inch taken beyond the visible cracks. The areas where covers were to be mounted also had their skin removed as originally planned. Excess adhesive was then removed, and the exposed metal surfaces re-scored. Patching layups were then performed independently over the root (overlapping Bay 2), Bays 4 and 5 combined, and a small pockmark on the upper skin near the root and leading edge. To do these layups, Henkel EA 7000 .05M film

adhesive was laid over the surface where the skin removed, followed by two layers of the original fiberglass fiber in its original orientation (+/- 45 degrees from the elastic axis). Finally, a single ply of carbon fiber cloth (the same cloth used during the assembly layups, and also in the same orientation as the fiberglass) was laid with a 1 – 2 inch overlap beyond the removed skin. The original Epikote 135 resin was used during all patching layups, and the patched sections were placed under vacuum for 24 – 48 hours to cure. During the layups on the bottom surface, which required the full wing to be placed under vacuum again, further modifications were made. The rears of Bays 2 through 4 were reprinted with vertical support pylons and installed, and chunks of leftover foam were cut and placed in openings to support the vacuum bag. The patched areas on the bottom skin before and after the placement of the patches can be seen in Figure 25, and full views of the bottom surface after the patches and during flap mounting can be seen in Figure 26.

Figure 25: Patched surfaces on bottom surface before (left) and after (right) patching layups

Figure 26: Wing with patches during flap mounting (left) and early GVT testing (right)

With the patching complete, standard Bondo body filler was applied and sanded by hand to smooth the OML and fill out the LE. Thus, the Bondo was mostly concentrated at the LE, TE of the fiberglass, and over the carbon fiber patches. In total, approximately 3 pounds of Bondo remained on the wing after sanding. With the sanding complete, the wing was then painted. The wing was painted with three coats of Rust-Oleum Automotive Filler Primer (high build, pintura base) to fill imperfections, two coats of Rust-Oleum Painter's Touch 2X Ultra Cover Paint + Primer (satin charcoal gray for the wing body and flat black for the flaps), and finally two coats of satin clear coat (same type as the paint). Satin finish was selected in order to provide a non-reflective surface for the Vicon system.

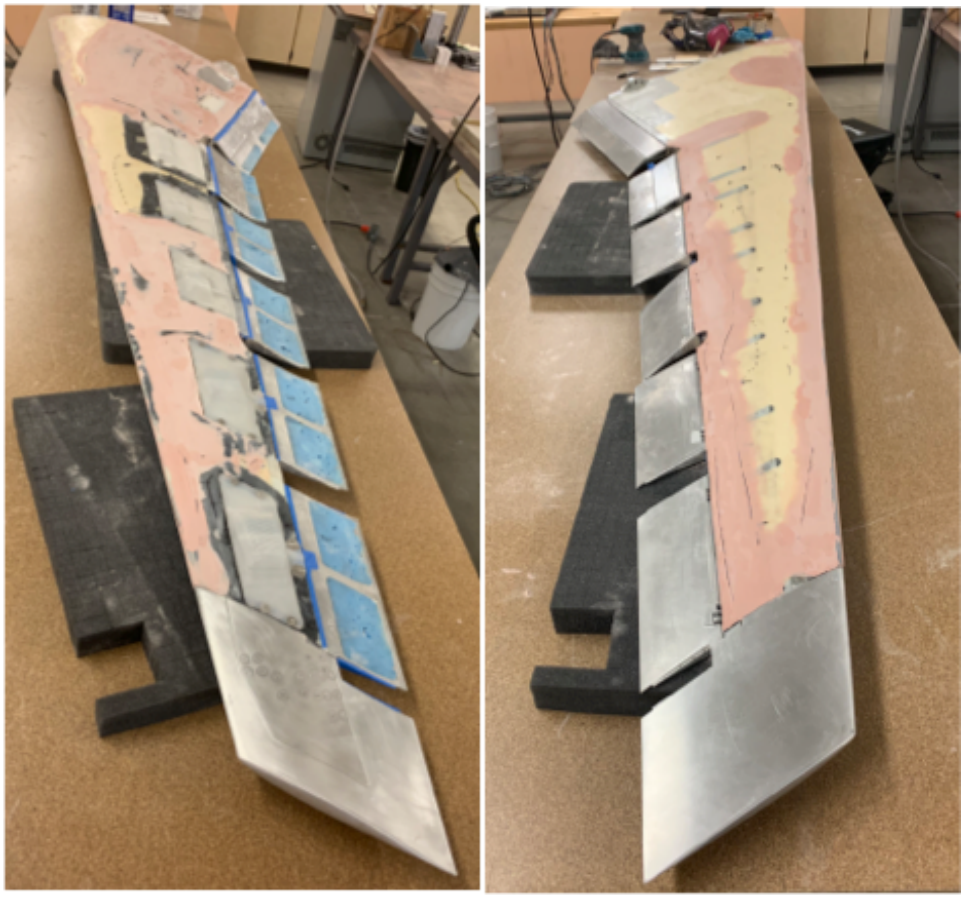

Figure 27: Lower (left) and upper (right) surfaces after Bondo application and sanding

6. ACTUATOR SELECTION

As the drive screw actuation style of Wing III was too slow to operate for GLA, a new actuation style was selected. In order to maximize speed, one- and two-bar linkages (for the single- and double-jointed flaps respectively) were pursued as a replacement. Preliminary aerodynamic models placed the required load capacity of a direct-drive servo between 200 and 400 oz-in. Similarly, a speed requirement of over 300 degrees per second was chosen in order to meet expected gust response requirements. Travel range for the linkages required at least 90 degrees of operation, and the actuator needed to minimize geometric size and stall current. Metal, rather than plastic, casings were preferred after damage seen in the original servos of Wing III.

Ultimately, three servos were selected for validation and testing. The first, an MKS HBL599, was selected due to the favorable experience with MKS wing servos as replacements in Wing III. The Hitec HSB-9381TH and Dynamixel XM430-W210-R were selected based on experience with the brands in previous, unrelated projects. The published performance and size of these three servos are listed in Table 3. The Hitec had the lowest range, at 158 degrees, and the highest stall current, at 2.7 A.

Table 3: Tested Servos with Published Specifications

Brand	Model	Max. Torque	Max. Speed	Size (HXWXL)	Voltage	Weight
		oz-in	deg/s	in	VDC	oz
MKS	HBL599	527	667	1.57 X 0.79 X 1.52	7.4	2.58
Hitec	HSB-9381TH	472	429	1.57 X 0.78 X 1.50	7.4	2.40
Dynamixel	XM430-W210-R	425	462	1.83 X 1.12 X 1.34	12	2.89

To validate these specifications, a test rig was designed and built that can be seen in Figure 28. This rig used T-slot block and slotted components to allow the mounting of different servos. An aluminum bar with slots at 1.25, 1.75, and 2.5 inches from the rotation axis was attached to a servo horn, along with a Bourns PTD901-1015F-B203-ND potentiometer. The potentiometer's analog signal was put through a low-pass filter with a cutoff frequency of 48.2 Hz, and then read by an analog pin on an Arduino Due at approximately 242 Hz. Servos were given their supply voltages from a dedicated power supply with a 4 amp limit, and signal was provided directly by a digital output pin on the same Due. The Dynamixel was an exception to this control scheme as it was commanded by an OpenCM9.04C and powered by an OpenCM 485 Expansion Board. The Dynamixel was a digital servo, and required the listed boards (produced by the same manufacturer) and its own software to control. The Due still read the external potentiometer for the Dynamixel. A McMaster-Carr 9432K118 extension spring was attached between a separate plate and one of the slots in the aluminum bar in order to provide a torque resistance. To operate, a deflection angle would be commanded, and the

achieved angle, read by the potentiometer, would indicate the torque achieved based on the slot the spring was attached to.

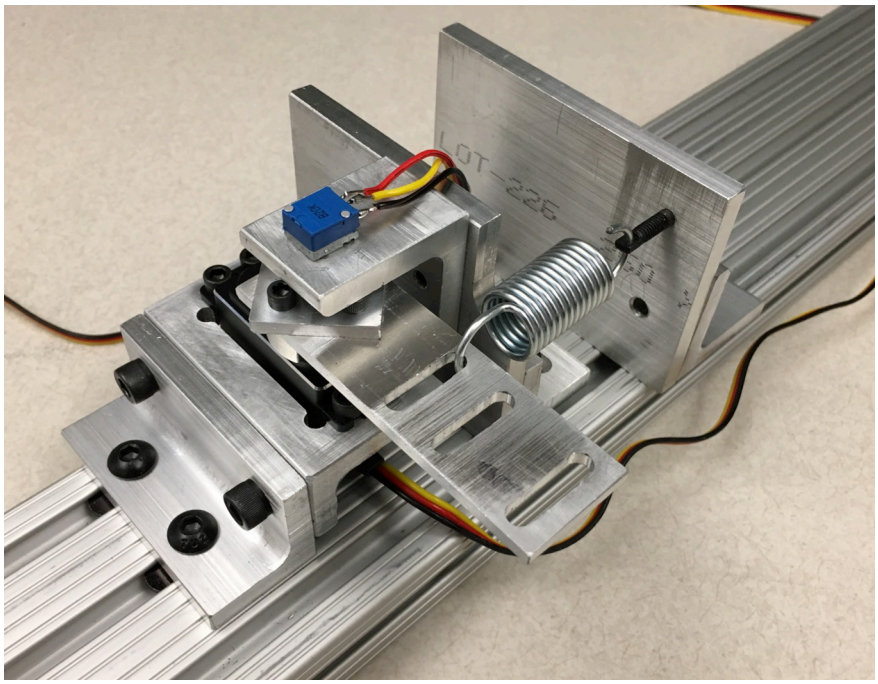

Figure 28: Actuator test rig

Prior to testing the servos, the spring and potentiometer were tested separately for linearity. These results are shown in Figure 29 and Figure 30 for the spring and potentiometer, respectively. The spring, quoted at 14.1 pounds per inch, had a resistance of 16.96 pounds per inch and a linearity of approximately 2% over its full extension. The potentiometer had a resolution of 5.09 counts per degree, and a linearity of about 3% over 70 degrees of travel.

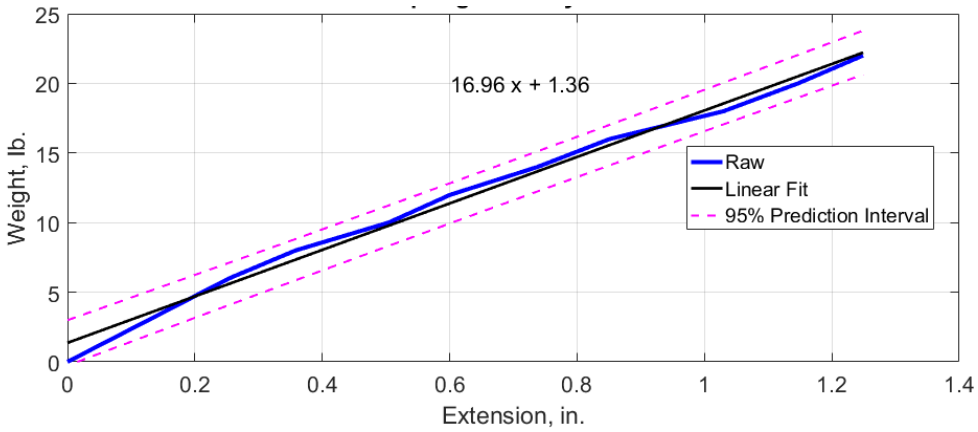

Figure 29: 9431K118 spring linearity test results

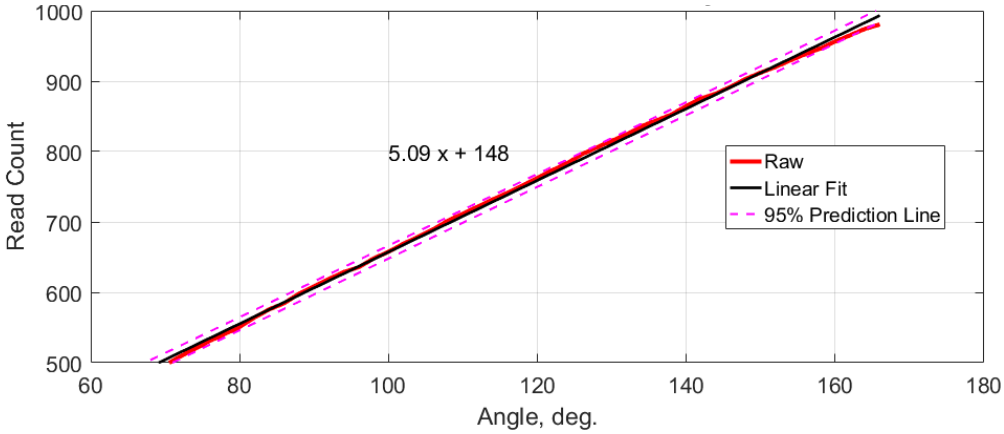

Figure 30: Bourns potentiometer linearity test results

Initial servo testing used ten, 1-second interval steps to a prescribed deflection (ranging between 5 and 50 degrees), with the spring varied between the three slots. An example output comparing the same test run for the three servos is shown in Figure 31. In this example, the Hitec (blue), Dynamixel (red), and MKS (magenta) servos were all run with open loop control. As the Dynamixel-specific software allowed quick alterations to its internal PID control, this run was included (in black). The PID gains used here were 15,000 for P, 15,000 for I, and 5000 for D (out of a possible 16,383). This was designated as “G8 gains.”

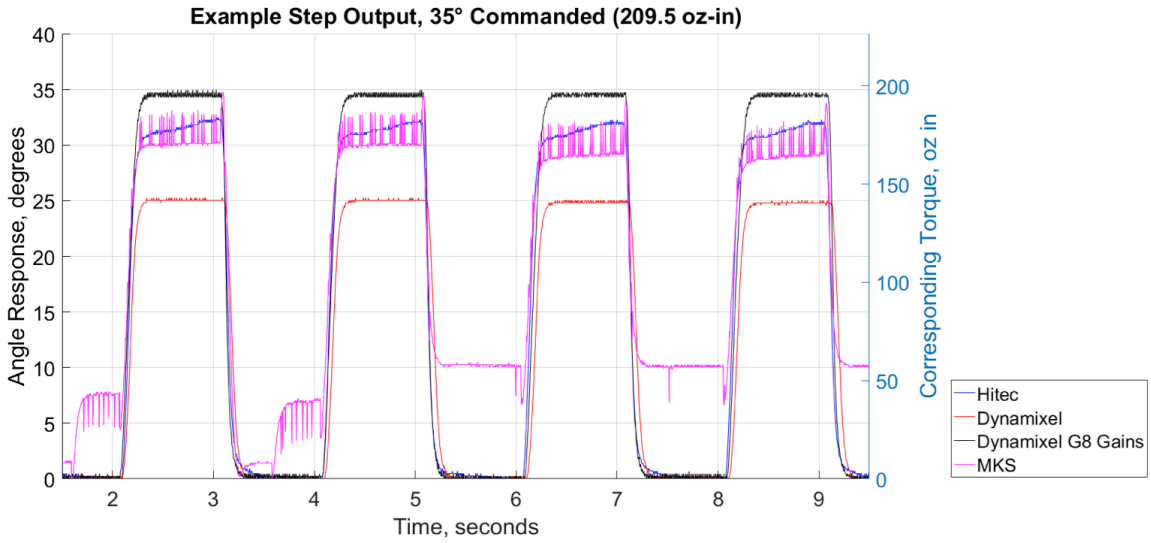

Figure 31: Open-loop actuator step response

Looking at the open-loop response, it immediately became clear the MKS would be inadequate. It tended to chatter (a phenomena seen, but originally misunderstood and ignored in the slower Wing III), and had a torque response that was significantly less than the published or required value. Thus, it was abandoned as an option for further testing. The Dynamixel preformed exceedingly well in initial runs, but for the Hitec to be comparable, it needed to also run with PID control.

A PID loop was added to the Arduino Due code, and the Hitec was tuned unloaded to gains of 200 for P, 2 for I, and 0 for D. The step command tests were then re-run. A repeat of the previous step response, but with closed loop control, is shown in Figure 32. The compiled and averaged results of the spring attached to the three different slots are shown in Figure 33. Here, the low torque indicated the shortest slot at 1.25 inches. Finally, Figure 34 shows a magnified response comparison of the medium torque range with respect to achieved torque. An important output from the latter two plots was the high torque response of the Hitec versus the Dynamixel. The Dynamixel became completely inoperable after approximately 225 oz-in (just over half its rating), whereas

the Hitec continued to operate, and actually showed improve response, beyond this point, up to 625 oz-in (almost one and a half times its rating).

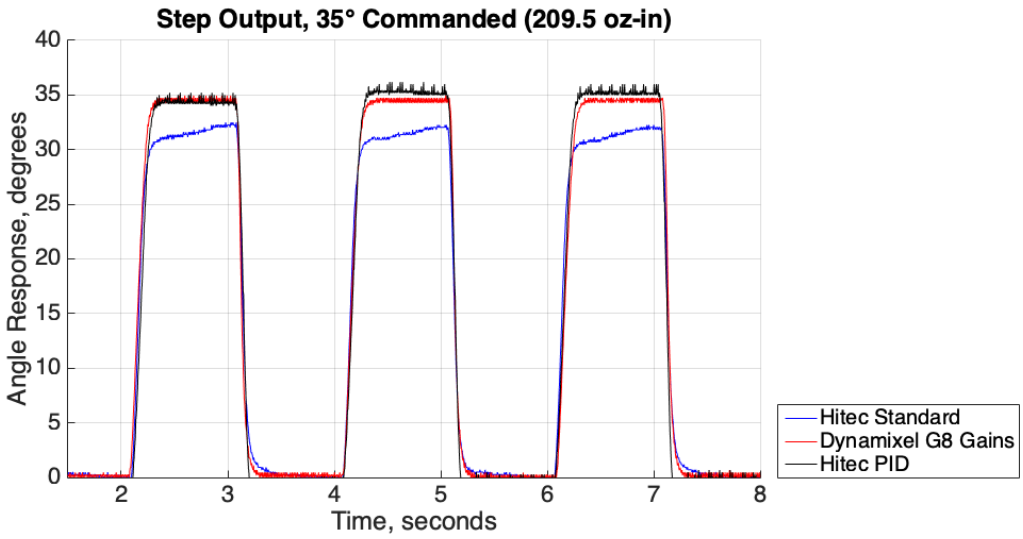

Figure 32: Closed-loop actuator step response example

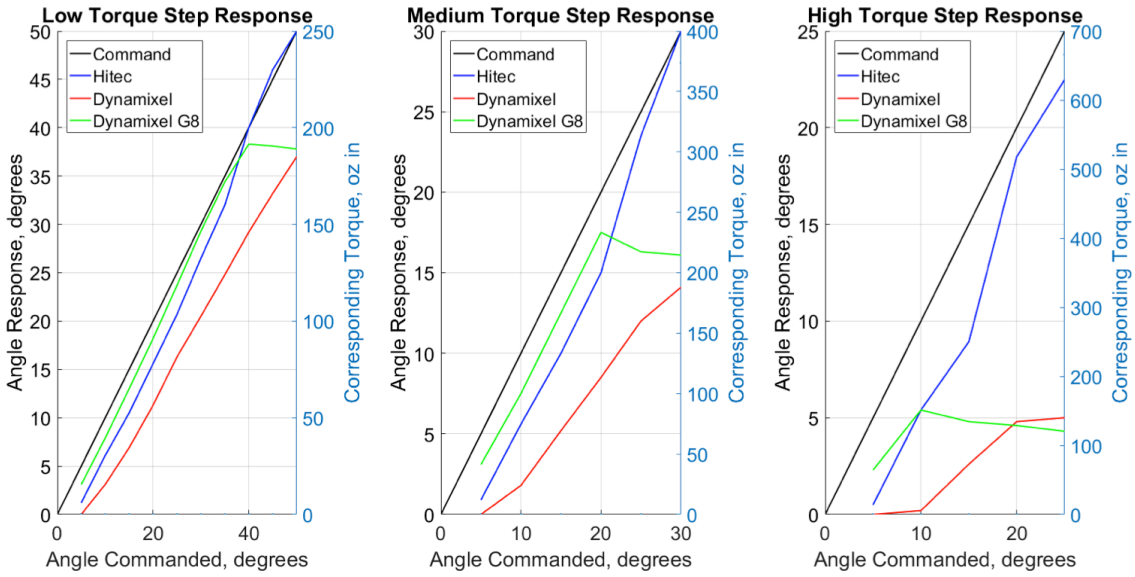

Figure 33: Averaged closed-loop step response results

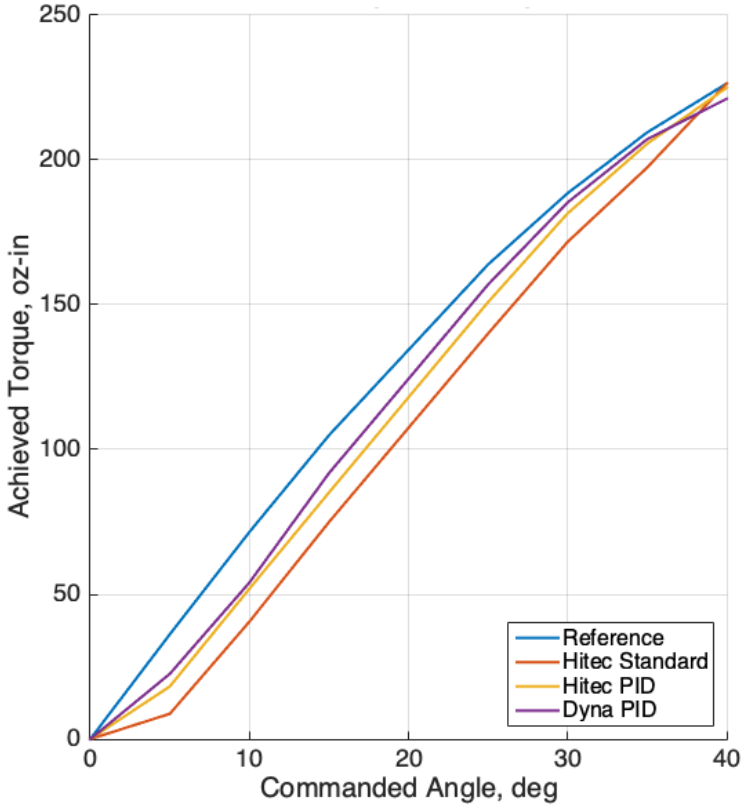

Figure 34: Medium torque actuator step response comparison

To provide complete a complete view of these actuators, a frequency response comparison was also conducted. The same setup and PID values were used as the step response tests, but the servos were commanded in a sine wave at increasing frequencies. The averaged results are shown in Figure 35. The Hitec was reliable up to approximately 2.5 Hz, and the Dynamixel up to 4.25 Hz.

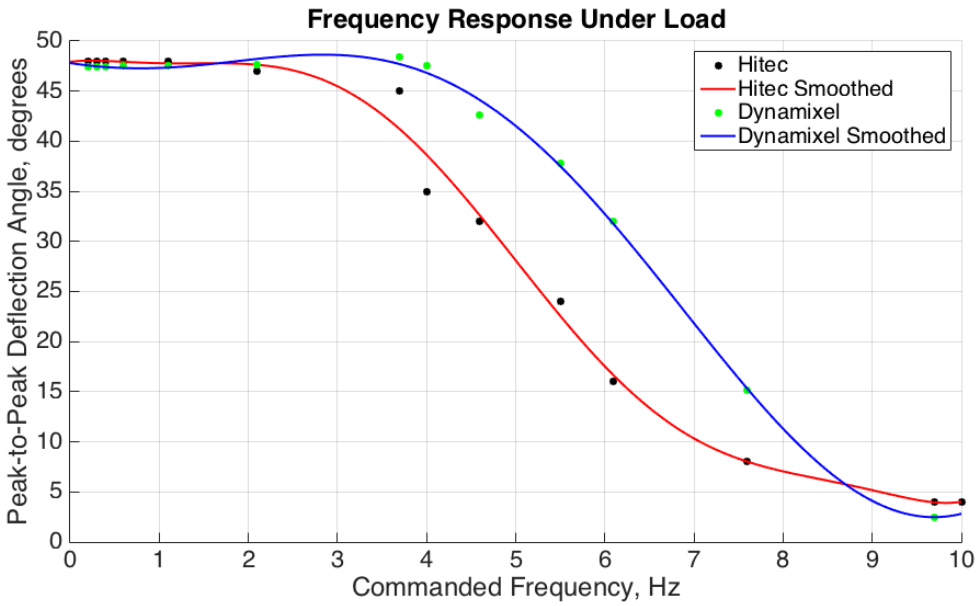

Figure 35: Hitec and Dynamixel averaged frequency response

Using all the data from actuator testing, the Hitec was selected for installation into the wing. The Hitec utilized a smaller casing and could be readily integrated into the code and wiring of Wing III, whereas the Dynamixel required its own language and hardware, increasing cost and development time for the system. The Dynamixel also lost its holding ability if power was lost, whereas the Hitec was hard to back drive when unpowered. This would be beneficial for the direct linkages planned for the wing, both in terms of reducing the amperage load on the power supply and preventing damage if power loss were to occur. Finally, while the Dynamixel showed a more promising frequency response, the torque response of the Hitec covered the entire range of expected loads. This was especially important since, at the time of actuator testing, there was significant uncertainty in the load estimates. The 2.5 Hz response of the Hitec was adequate to control the first bending frequency of Wing IV, which ended up near 2 Hz.

7. ACTUATION DESIGN

The actuation of Wing IV is a combination of single- and double-jointed flaps. With exception to the OML and span, Bays 1 and 2 used an identical double-jointed actuation design, and Bays 3 through 6 used a single-jointed design. Both flap styles mounted to the ribs using 90-degree ball type rod end bearings (MISUMI RBLD4). These allowed the ribs to attach to the flap and remain decoupled, which increased flexibility and removed the constriction on deformation imposed by the flap wells of Wing III.

The single-jointed design used a centralized servo to drive the flap through a simple one-bar linkage. A 6-32 threaded rod connected two ball joint rod ends (McMaster-Carr 60645K78) attached to the metal servo horn and the flap. Each of the three mounting points (two to the rib, one to the servo) was detachable, and since the servo was attached to the spar with an access cover, repairs and replacements were quick and straightforward. A CAD image of the single-jointed actuation design with the main flap body and cover transparent is shown in Figure 36, and Figure 37 shows a view of Bay 4 assembled and painted during wiring.

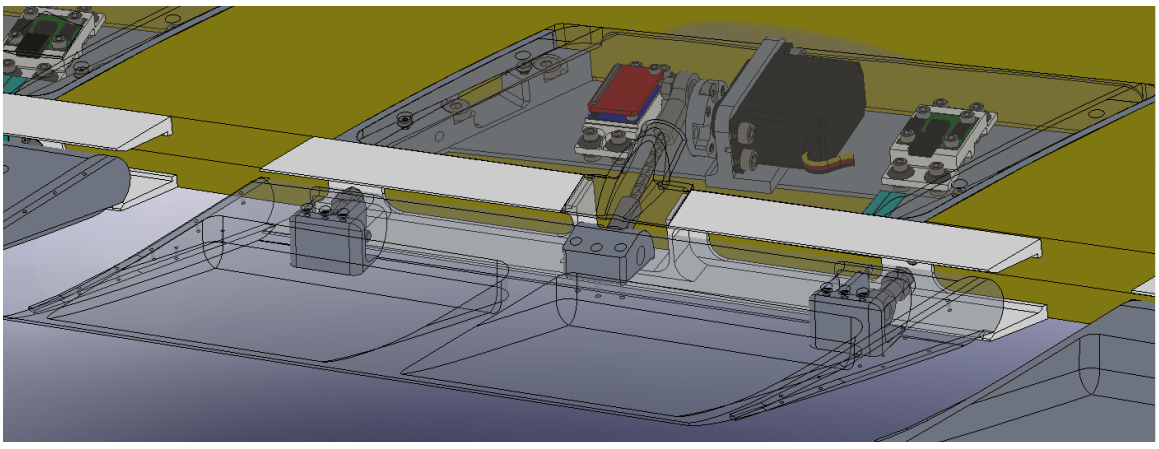

Figure 36: Bay 4 single-jointed flap CAD view

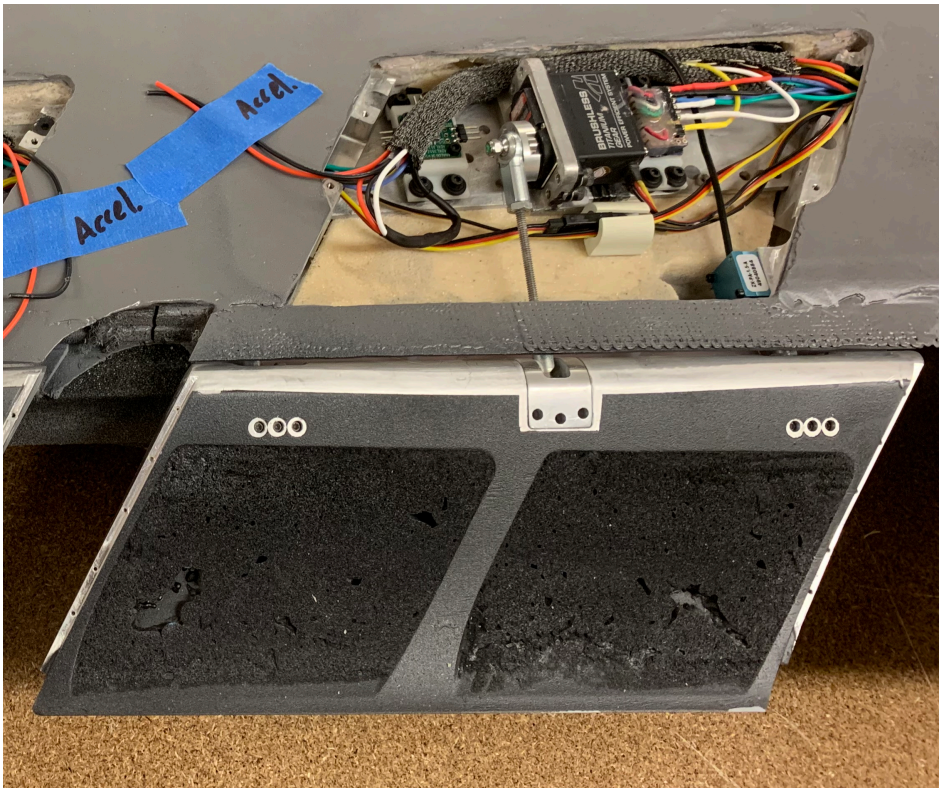

Figure 37: Bay 4 single flap during wiring

Double-jointed flaps utilized two servos to drive the independent surfaces, both of which were mounted to the spar. The A-sides used an identical one-bar linkage to the single jointed flaps. The B-sides were actuated using a two-bar linkage, with the connection between the linkages attached to a pair of miniature linear rails (McMaster-Carr 8381K39) mounted in the hollowed-out space of the A-side. A CAD representation of the double-jointed Flap 2 from an early test rig can be seen in Figure 38, and an image of the inside of Flap 2A with the mounting points and linear rail exposed is shown in Figure 39. A small amount of coupling was seen between the A- and B-sides during operation when run in open loop, but was corrected when using closed-loop control.

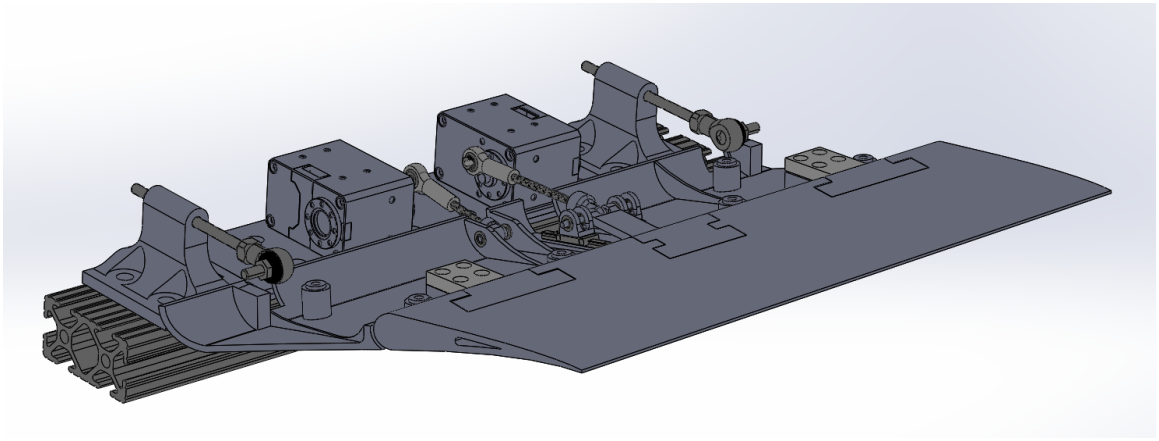

Figure 38: Bay 2 early double-jointed flap test rig

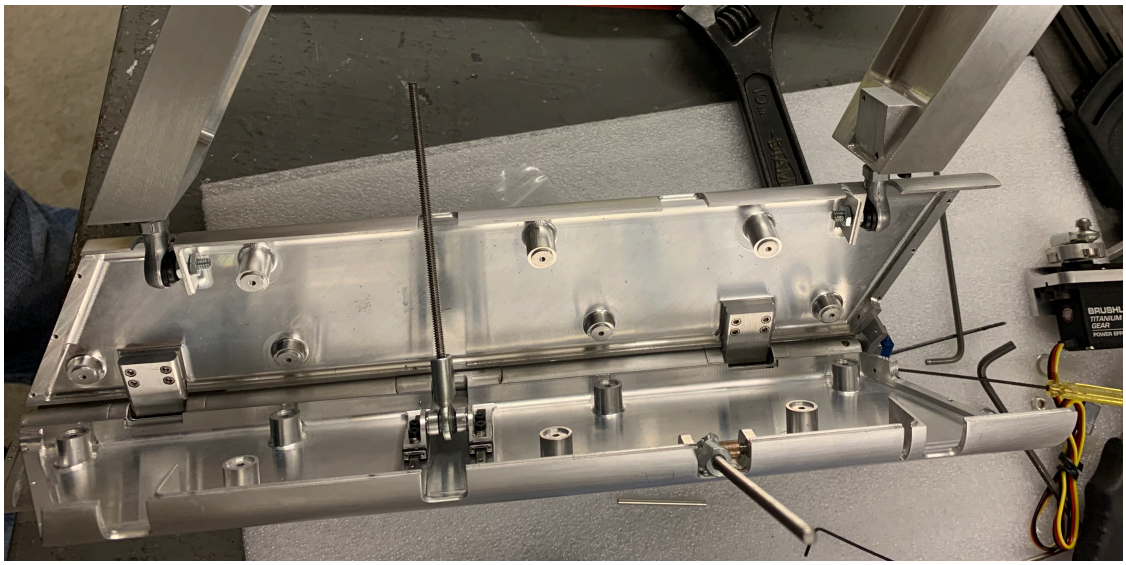

Figure 39: Flap 2A open clamshell view during assembly

Position sensing for the single-jointed flaps and A-sides was accomplished using a miniature string potentiometer. The potentiometer body was mounted to the inner rib, and a wire with an eyelet was run to the rotation axis of the flap. The connection was slightly offset from the rotation hinge, such that whenever the flap moved, the wire was pulled and the string potentiometer rotated internally, producing an analog signal change like a typical potentiometer. A large benefit of this system was the absolute, rather than incremental, measurement system, which improved repeatability. It also did not get in the

way of the decoupled ribs. Since the measurement was taken directly at the rotation axis, any movement related to mechanical slop or load was seen by the system, improving the closed loop control. B-side positions were measured using standard potentiometers mounted to the sides of the flaps.

Weight reliefs were cut into the bottom surfaces of single-jointed flaps and B-sides. These were filled with Duo Fill 400 expanding insulation foam. After sanding and painting, the leftover surface was rough and contained voids, and was thus covered by aluminum tape during testing.

8. FLAP CONTROL SYSTEM

The actuation of each bay was handled independently from one another, but shared common power supplies. Command generation and control loop processing occurred off-wing, and used the I^2C communication protocol to read and control the position of each flap. A high-level schematic of this system is shown Figure 40, and shows an example of both single- and double-jointed bays. The flap control system was designed by SSCI, with wiring and implementation accomplished by the University of Washington. Troubleshooting was a joint endeavor led by the University of Washington, with assistance provided by both SSCI and NASA.

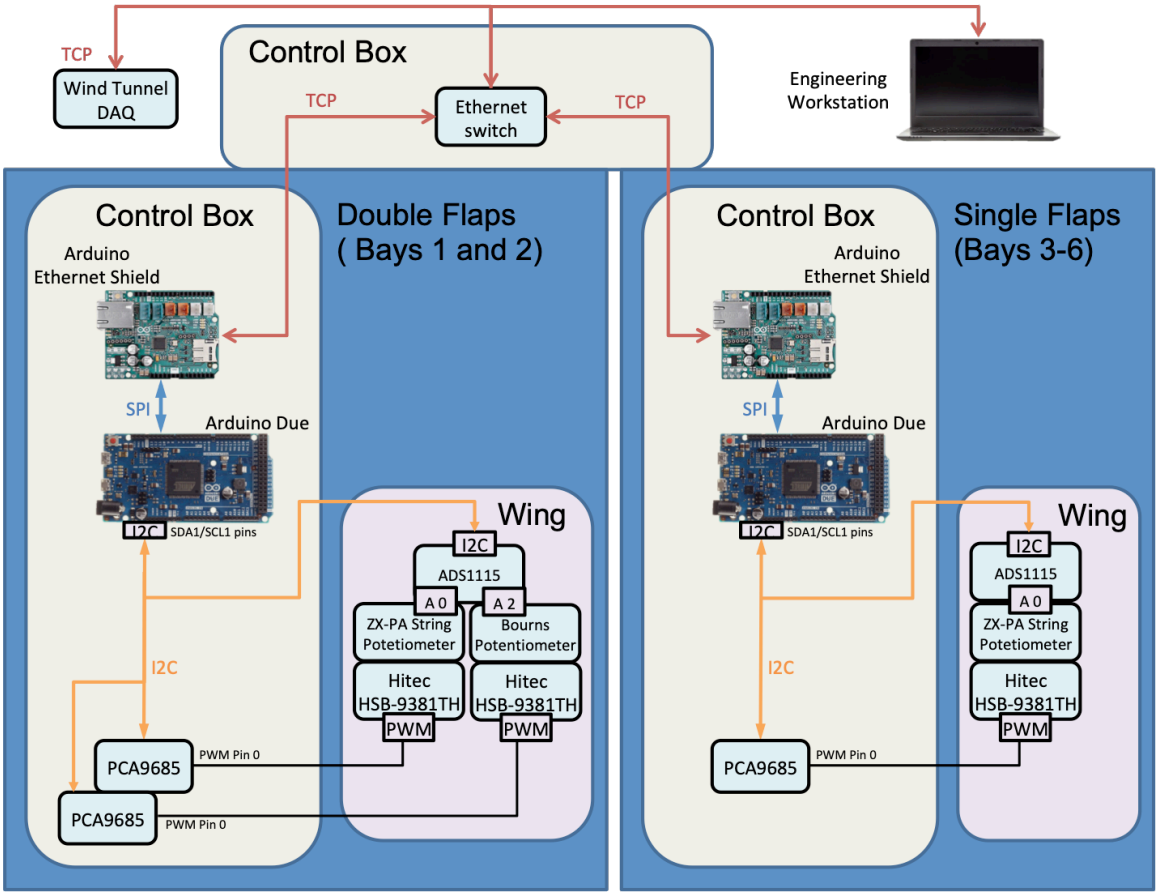

Figure 40: Flap actuation system schematic

For each bay, a single Arduino Due (the master) managed the slaves of its I^2C bus, which included a single analog to digital converter (ADC) per bay, and one servo driver per servo. Each ADC was an Adafruit ADS1115, and the Adafruit PCA9685 was selected as the servo driver. The ADC was operated using differential reading, and thus could handle up to two analog position signals. These analog signals were generated using either a Unimeasure ZX-PA-1.5-APN string potentiometer (single-jointed flaps and A-sides) or the Bourns potentiometer used in actuator testing (B-sides). Prior to the ADC, the analog signals were passed through a 48.2 Hz low-pass filter identical to the one used in actuator testing.

To operate the system, an engineering workstation, developed by SSCI, received force and moment data from the wind tunnel's sidewall balance and generated a command for each bay. These were sent out through TCP and were read into the Due by an Arduino Ethernet Shield 2. The Due would then command the servo driver over I^2C, which would command a PWM signal to the Hitec servo. The servo would execute this command, and the motion would be read by the potentiometer. The ADC would then read the potentiometer signal and send the position data back to the Due over the common I^2C lines. The Due was then in charge of achieving and maintaining the commanded position using a standard PID loop. PID was conducted on the potentiometer feedback, as this reflected actual position (including any mechanical slop), and was then converted to the PWM command sent to the servo driver using a third order polynomial fit. The PID gains were tuned manually and independently for each flap, and the fit was made from flap calibrations done prior to testing. The Due could only receive commands through either the workstation or the serial monitor of the Arduino IDE (which required USB

connection to a separate computer), and each bay ran completely independent of the others.

For power, all ADC, potentiometers, and servo drivers were supplied by a dedicated 3.3 VDC power supply. The ADCs were also supplied with 1.1 VDC, divided out from said power supply using resistors, in order to perform differential readings. Servos were supplied 7.4 VDC from three Mean Well RSP-320-7.5 power supplies. No more than three servos were attached to each power supply. The control box also possessed a dedicated 12 VDC power supply to run the cooling fans and 8-port Ethernet switch. Arduinos were powered by a single 9 VDC, 650 mA wall wart.

Power and communication was run to the wing using three separate, shielded wire bundles. The first contained the independent power, ground, and signal wires of the servos. The second contained the data and clock lines for the ADCs, and the final bundle contained the 1.1 VDC, 3.3 VDC, and ground wires common to all ADCs and sensors. An Ethernet and USB cable were also run for the load sensing system, described in the next chapter.

The off-wing components were mounted into a single control box. This included all power supplies, the six Arduino Dues with their Ethernet shields, and the eight servo drivers. The box also included the Ethernet switch, a USB hub, cooling fans, external connectors for both AC power and the wing wire bundles, and power isolation switches for the sensors and servos of each bay. An image of the control box can be seen with a separate computer testing an Arduino through USB during troubleshooting in Figure 41.

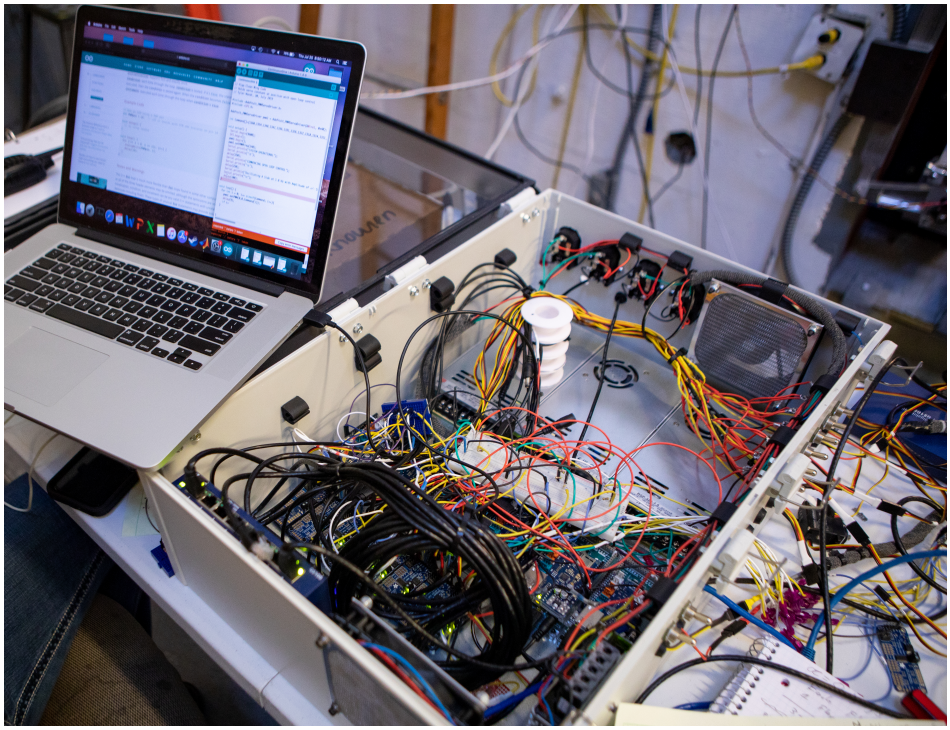

Figure 41: Control box during troubleshooting (photo courtesy Matt Hagen)

9. LOAD SENSING SYSTEM

The load sensing system utilizes six accelerometers and three strain gauge stations to determine wing motion and loading. This system has a dedicated in-wing Arduino Due, and, like the flap control system, utilizes the I^2C communication protocol. A high-level schematic, which runs parallel to and independent of the flap control system, is shown in Figure 42. Like the flap control system, the load sensing system was designed by SSCI and implemented by the University of Washington.

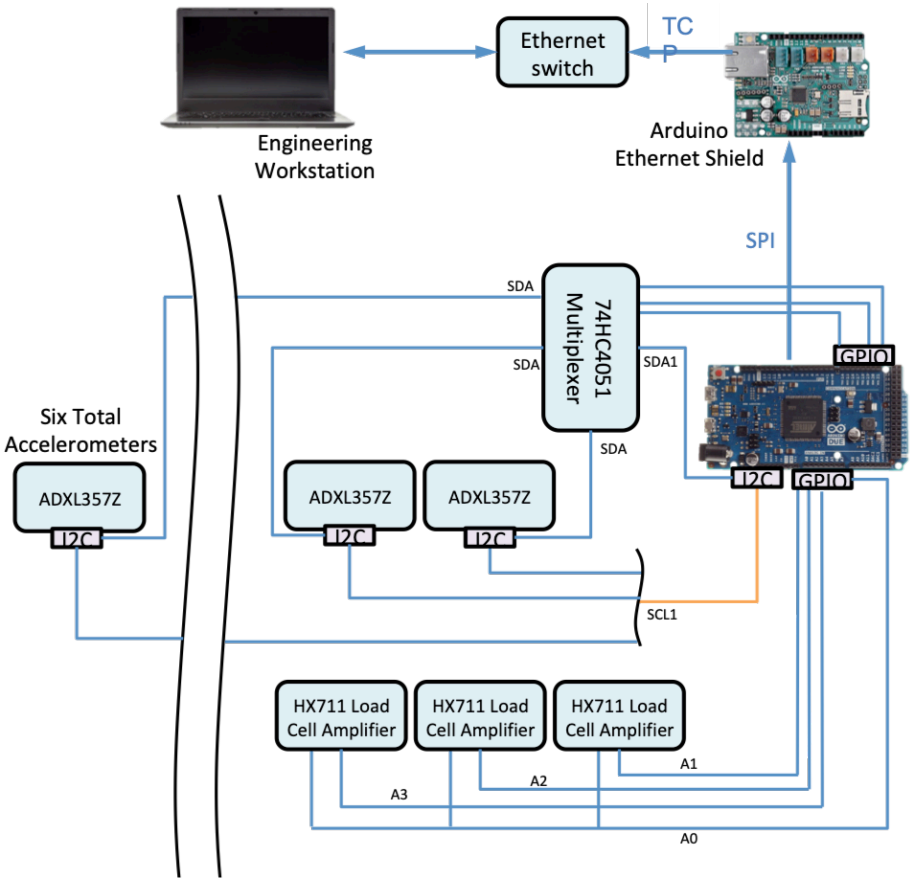

Figure 42: Load sensing system schematic

The ADXL357Z by Analog Devices, Inc. was selected as the accelerometer due to its range and sensitivity. The "Z" indicates the evaluation board, rather just the chip itself, was used. This contained necessary capacitors and resistors for the chip, provided

pin outs for the use of headers, and provided mounting holes directly on the PCB. Two Omega SGD-3/350-DY13 strain gauges were used on the upper and lower surface of the spar at each station, and were wired into a Sparkfun HX711 load cell amplifier in a half bridge configuration. A Sparkfun 74HC4051 multiplexer breakout was used on the accelerometer data lines in order to solve I^2C addressing issues. All sensors and the multiplexer shared the 3.3 VDC power supply lines used by the flap control system.

Sensor placement was driven by geometric constraints. Sensors were mounted on the bottom surface of the spar along its centerline wherever space remained after mounting the actuation components. The exception to this rule was the two tip accelerometers, which were purposefully offset from the elastic axis to catch twisting motion. The position in which these sensors were mounted is described in Table 4. The distance along spar is to the center of the sensor from the root plate, the vertical offset is from the bottom of the spar to the bottom of the sensor PCB, and the LE offset is the distance towards the LE along the local chord away from the spar centerline. It should be noted that the tip accelerometers are inverted, and thus the body of these sensors were closer to the spar, not further away like the other sensors.

Table 4: Sensor Positions

Sensor Type	Bay	Distance Along Spar	Vertical Offset	LE Offset
Accelerometer	3	49.60 in	0.3825 in	0 in
	4	59.75 in	0.3825 in	0 in
	5	72.82 in	0.3825 in	0 in
	6	84.98 in	0.3825 in	0 in
	Tip LE	93.78 in	-0.2725 in	1.44 in
	Tip TE	93.78 in	-0.2725 in	-1.44 in
Strain Gauge	Root	2.08 in	0 in	0 in
	2	32.29 in	0 in	0 in
	4	61.87 in	0 in	0 in

For the accelerometers, ADCs, and HX711 amplifiers, vibration-isolation mounts were designed and installed. The mounts were made from 3D printed trays that were then mounted to press-fit nuts on the spar through vibration isolation grommets (McMaster-Carr 9307K156). The boards themselves were rigidly bolted to these trays. Clearances were maintained to ensure the boards would remain electrically isolated from the wing. The trays were printed using stereolithography, and used Accura Xtreme White 200 as the material. An ADC and accelerometer, along with a servo and the wire bundle, can be seen in the completed wing in Figure 43.

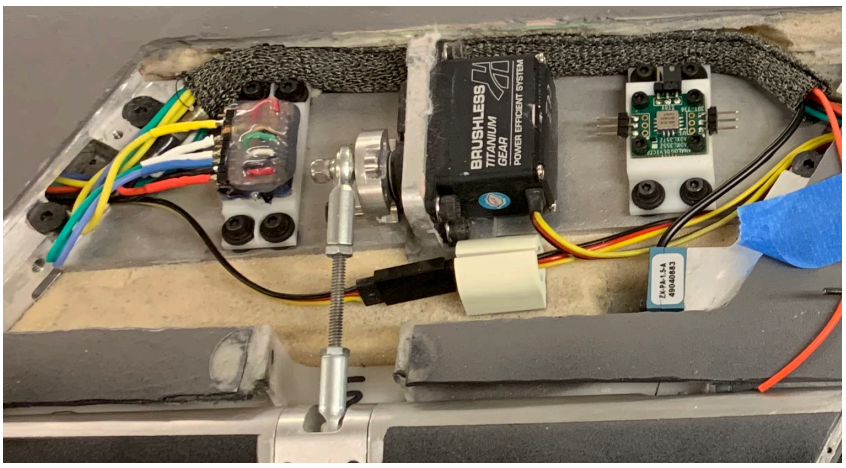

Figure 43: Bay 6 mounted sensors and actuator

10. MATHEMATICAL STRUCTURAL DYNAMICS AND AEROELASTIC MODELING

Accurate mathematical models of the structure, dynamics, and aeroelastic behavior were necessary to guide the development of Wing IV and provide control system designers with the models required for the generation of control laws for the system. These models then guided hardware development to ensure the design would meet design goals, while preventing failure throughout the planned testing envelope. As previously mentioned, achieving as low of a first bending frequency as possible was a high priority to ensure the structure's gust response would be within the frequency range of the chosen actuators. Another important goal was to create easy access to a large section of internal volume of the wing for system maintenance and repair, while also maintaining structural integrity under both steady and dynamic loads.

Wing IV's design included foam, fiberglass skins, and a metal spar bonded together, with cutouts for access holes surrounded by carbon fiber reinforcements. Accurately modeling this design prior to assembly presented a significant challenge. To compound the issue, schedule and budget constraints did not allow for a prototype wing to be built and tested for fine-tuning the finite element model and identifying load limits and failure mechanisms.

To tackle this problem, a significant amount of information and experience was taken from the finite element modeling of the three previous VCCTEF wings built at UW (Wing I – Wing III). Material properties of the fiberglass skins and the behavior of a bonded skin / foam wing were reused, with adjustments made for the different foam and resin selected. To study the capability of a finite element model to capture the behavior of

a skin / foam structure carrying an internal spar with a trough for access, an old prototype, used for the development of Wing I, was used. A thin metal spar was inserted into a trough cut into the bottom surface and bonded to the foam. The spar location and size was scaled geometrically to match the planned spar size and location in Wing IV. The modified prototype was then tested for stiffness and modal information, and finally loaded to failure. The results were compared against the unmodified prototype, and used to study and fine-tune the performance of the finite element model of the system.

The modified Wing I prototype structure is shown in Figure 44. Figure 45 shows the prototype loaded during static deformation measurements (which was later taken to failure). Results from these tests were used in the preparation of the finite element model of the Wing IV.

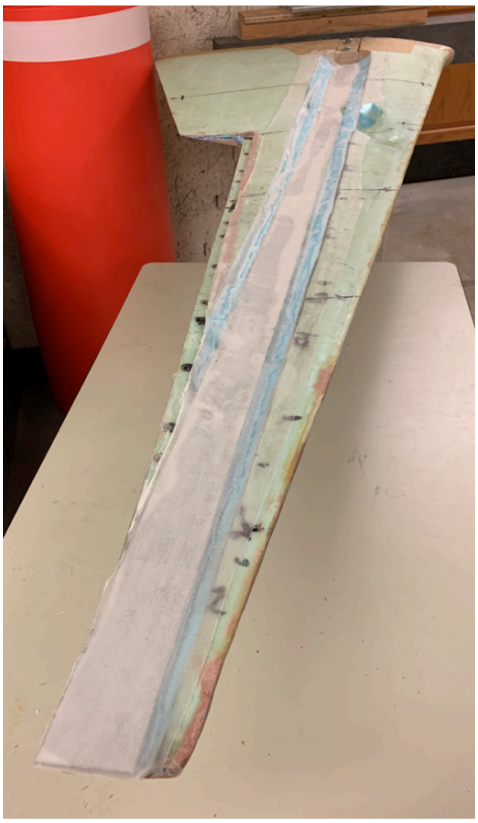

Figure 44: Wing I prototype with flat spar in access trough

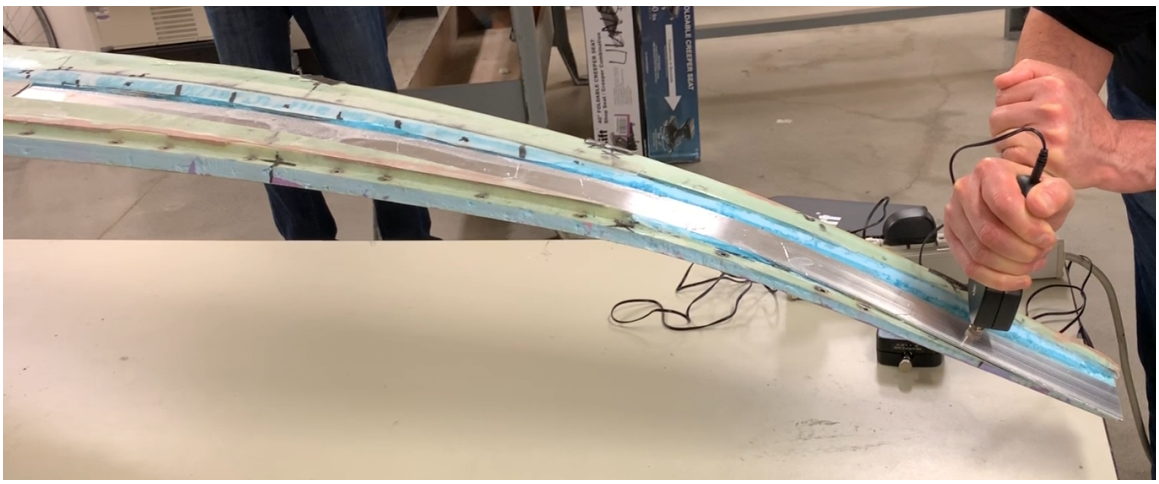

Figure 45: Prototype wing with spar and trough under static load

The finite element meshing of the upper surface of Wing IV (using FEMAP/NASTRAN) is shown in Figure 46. Note the metal root, tip, and control surfaces. The mesh of the lower skin of Wing IV is shown in Figure 47. Areas strengthened by the addition of carbon fiber cloth (both during assembly layup and patching layups) are shown in black. The access holes are shown in green. The foam, modeled using 3D elements, is shown in Figure 48. Two layers were used, which allowed the metal spar to pass between them. The pink sections represent cuts made for the ribs, which extended from the spar to the trailing edge to support the control surfaces. The ribs, along with the spar, were modeled using solid elements (like the foam) with the material properties of aluminum 6061-T6. The finite element mesh for the spar and ribs (the combination of which was called the aluminum pass) is shown in Figure 49. Finally, the Doublet-Lattice NASTRAN mesh is shown in Figure 50. The aerodynamic meshing of the flap segments are colored green, orange, and blue. Table 5 presents a summary of the characteristics of the NASTRAN finite element model.

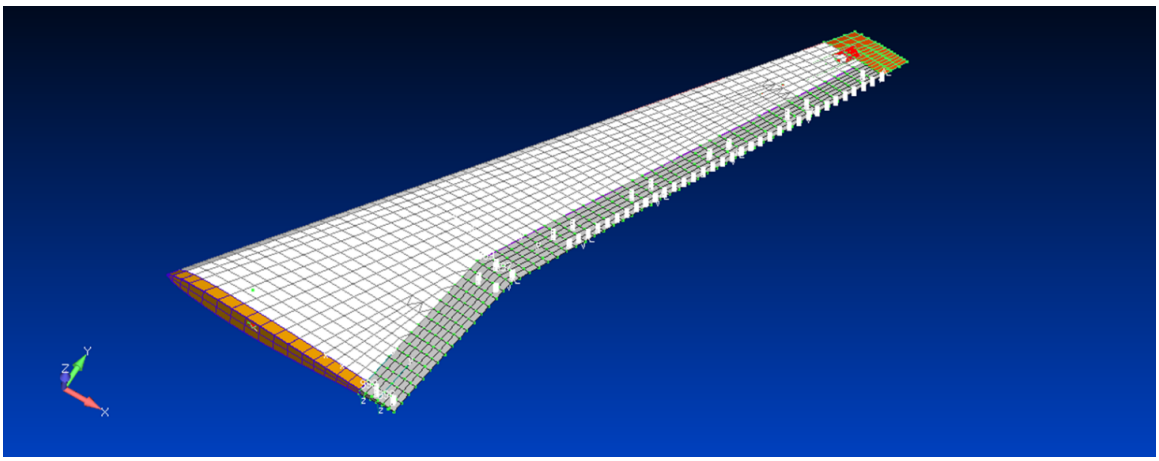

Figure 46: Finite element mesh of upper skin of Wing IV

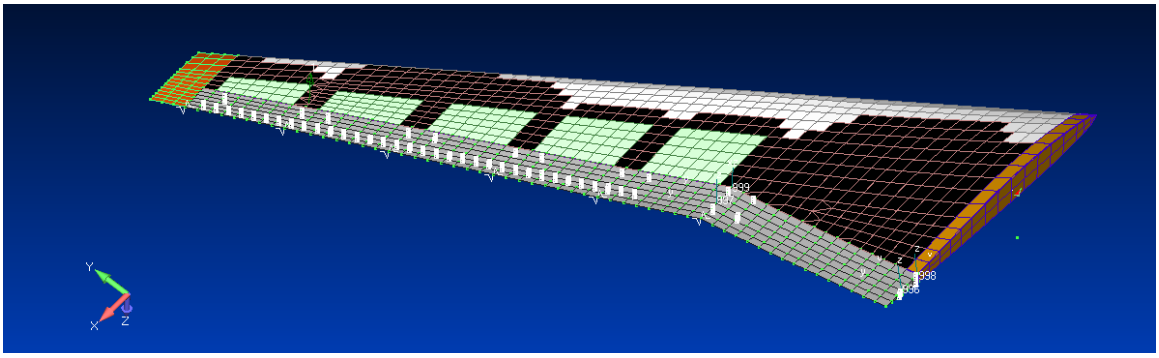

Figure 47: Finite element mesh of lower skin of Wing IV

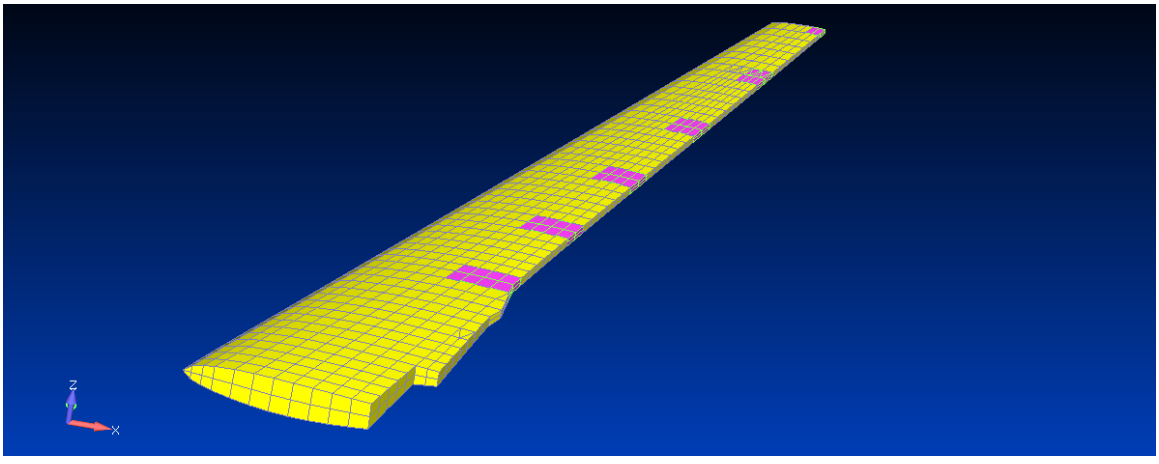

Figure 48: Finite element mesh of foam (layers of 3D solid elements) of Wing IV

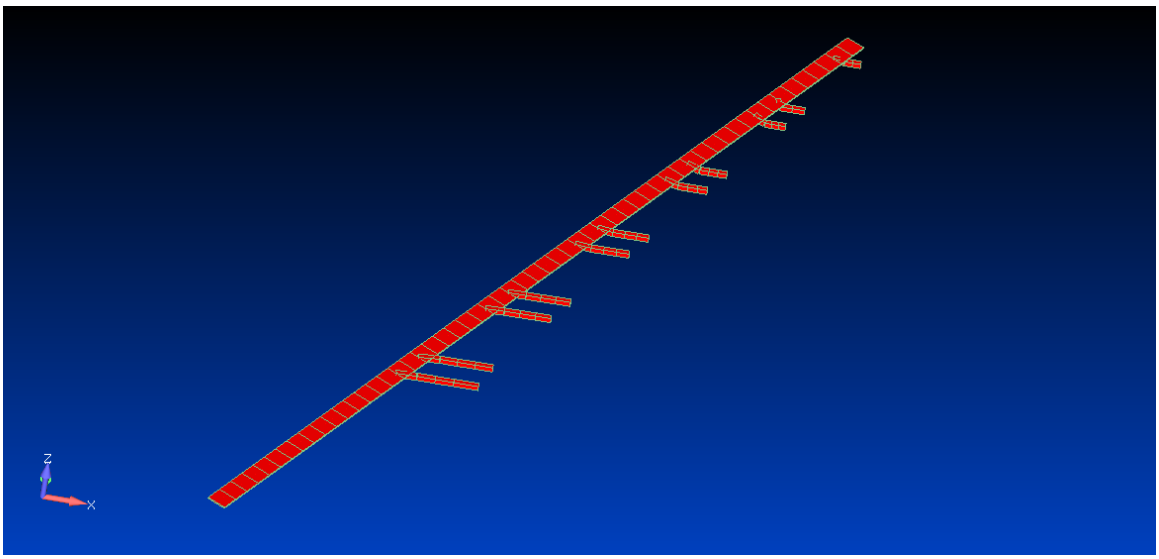

Figure 49: Finite element mesh of metal spar and ribs of Wing IV

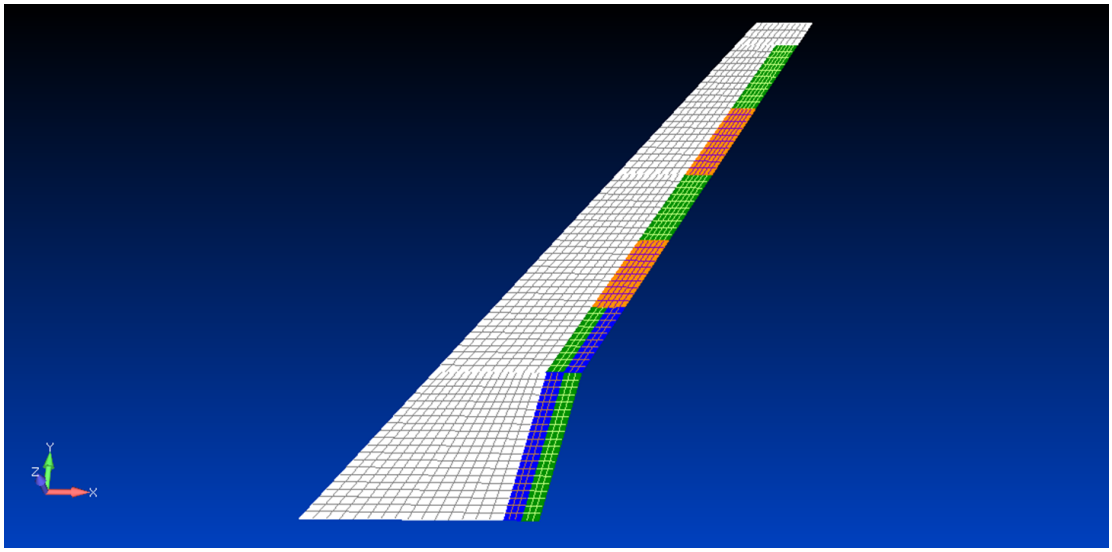

Figure 50: NASTRAN Doublet-Lattice aerodynamic mesh

Table 5: NASTRAN Model Summary of Wing IV

Number of Structural Elements	3322
Number of Aerodynamic Elements	1120
Number of Material Properties	13
Skin and Skin Reinforcements	Membrane elements w/ orthotropic material
Foam, Tip, Reinforcements	3D elements
Transition Strips	Spring elements
Aluminum Pass	Beam elements

Modal and static load tests were carried out with the final wing while mounted to the sidewall balance. The NASTRAN model was fine-tuned based on the results of these tests. A comparison of predicted versus measured natural frequencies of the fine-tuned finite element model is shown in Table 6, and the corresponding mode shapes are shown in Figure 51. The lowest structural damping measured, by a log decrement technique, was 2.5% of the first bending mode.

Table 6: Measured and Predicted Natural Frequencies

Mode #	Measured (Hz)	NASTRAN (Hz)	Description
1	2.2	2.2	First Bending
2	9.4	9.4	In-Plane Bending
3	10-11	10.8	Second Bending
4	23	24	Bending + Torsion
5	30	29	Torsion

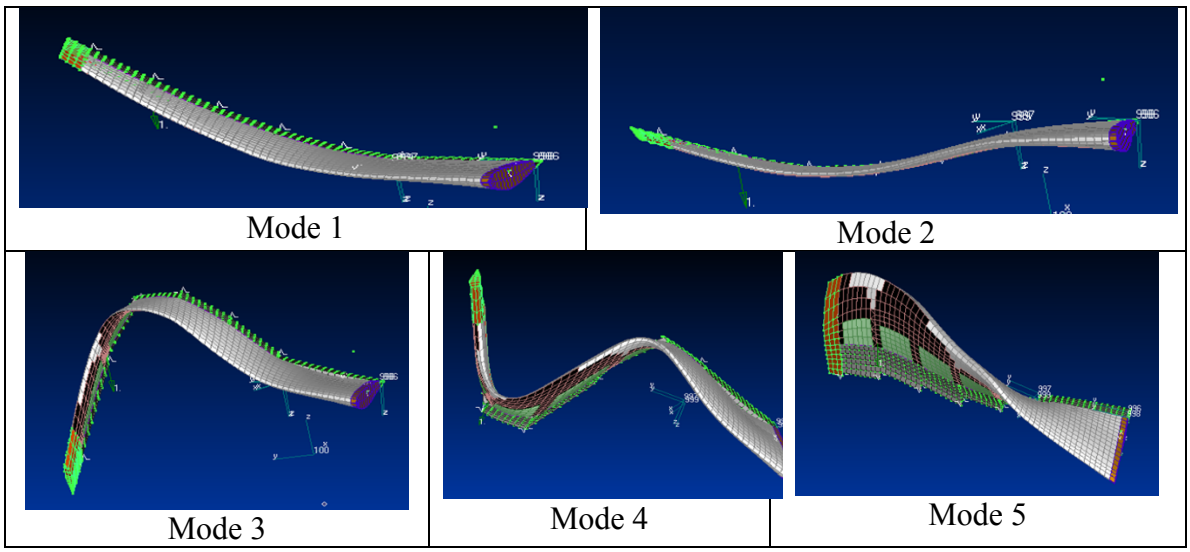

Figure 51: First five mode shapes of Wing IV

Flutter analysis was carried out for the flaps in a locked configuration. The NASTRAN p-k solution predicted two flutter mechanisms, shown in Table 7. The first predicted flutter mechanism had a frequency near Mode 2, which primarily dealt with in-plane motion. Therefore, the physical existence of this flutter mechanism is questionable, and the second mechanism, near Mode 4, is a more likely candidate. Regardless, the predicted flutter speeds were well above the planned testing range of 10 to 20 psf. The test envelope for the initial and shakedown tests stayed at 10 psf, and included a wide range of angles of attack and sinusoidal gusts (over a range of frequencies). During these, Wing IV was well damped and behaved.

Table 7: Predicted Flutter Mechanisms of Wing IV

Velocity (ft/sec)	Frequency (Hz)
335	9.5
321	18.5

Table 8 shows comparisons of measured versus predicted deformation results from static load tests. The corresponding load and measurement points are shown in

Figure 52. Overall, the correlation is adequate. However, additional tests with larger weights would be helpful. The loads used for the initial static load tests presented here were too low, and higher loads would permit the study of Wing IV's behavior from the linear range through nonlinear range.

Table 8: Static Loading Test and Deformation Analysis Comparison

Load & Location	Measurement Point	Measured (mm)	NASTRAN (mm)
2 kg Point 8	5	4	3
	6	6	5
	8	8	8
1 kg Point 10	8	6	5
	9	7	8
	10	8	9
1 kg Point 13	9	11	11
	10	15	13
	11	20	19

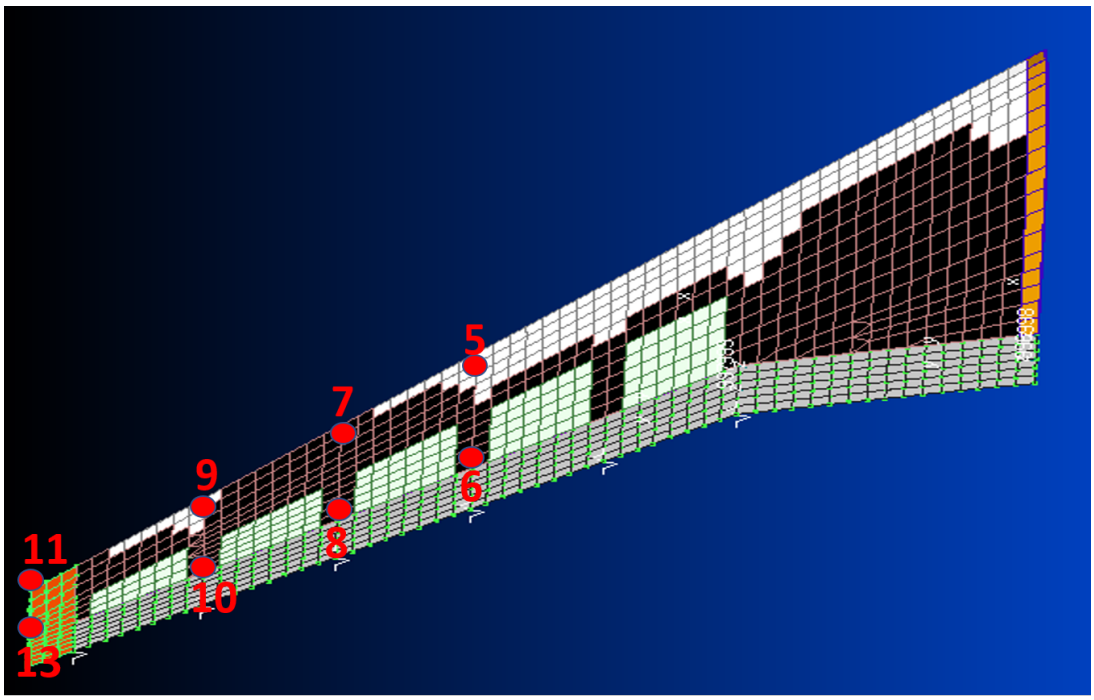

Figure 52: Static loading measurement points

Overall, the NASTRAN finite element model of the wing, coupled with the Doublet-Lattice model, was considered adequate. The resulting mass, stiffness, damping, and aerodynamic matrices would form the basis for the aeroservoelastic model of the wing, from which the control laws could be generated.

11. WIND TUNNEL TESTING

When testing in the Kirsten Wind Tunnel, the wing was rigidly mounted to a sidewall balance capable of reading the six reaction forces and moments. The lift, drag, and roll moment were of most interest during testing. The sidewall also executes commands for angle of attack changes from the wing's engineering workstation. A splitter plate is installed 6 inches from the tunnel wall in order to reduce the effect of the boundary layer on the wall of the wind tunnel. An image of Wing IV mounted in the wind tunnel with the splitter plate and gust vanes is shown in Figure 53.

Figure 53: Installed Wing IV and gust generator vanes showing splitter plate offset

Aeronautical Testing Service, Inc. (ATS) from Arlington, WA designed the gust generator system. The system was composed of four vanes of a NACA 0015 airfoil with a chord of 15 inches and a modified, wedge-like, TE. These vanes spanned the entirety of

the 12-foot test section. The vanes were hinged at the 0.3 chord point (approximately 4.5 inches), and this hinge was approximately 52.5 inches ahead of the sidewall balance's rotation axis. When the wing was mounted, the leading edge of the wing at the root was then 14.67 inches from the trailing edge of the vanes when both were at zero angle of attack. A single AC motor controlled the vanes. The mounting, actuation, and internal ribs of the vanes were made from aluminum, and the vane OMLs were made from carbon fiber. The gust generator is capable of oscillating with a 15-degree amplitude at up to 10 Hz. In testing, discrete 1-cosine and continuous sinusoidal inputs were typically used. The Kirsten Wind Tunnel crew also installed a position feedback encoder. A view of the gust generator motor, sidewall balance, control box, and operating computers as seen from the Kirsten Wind Tunnel's observation deck can be seen in Figure 54.

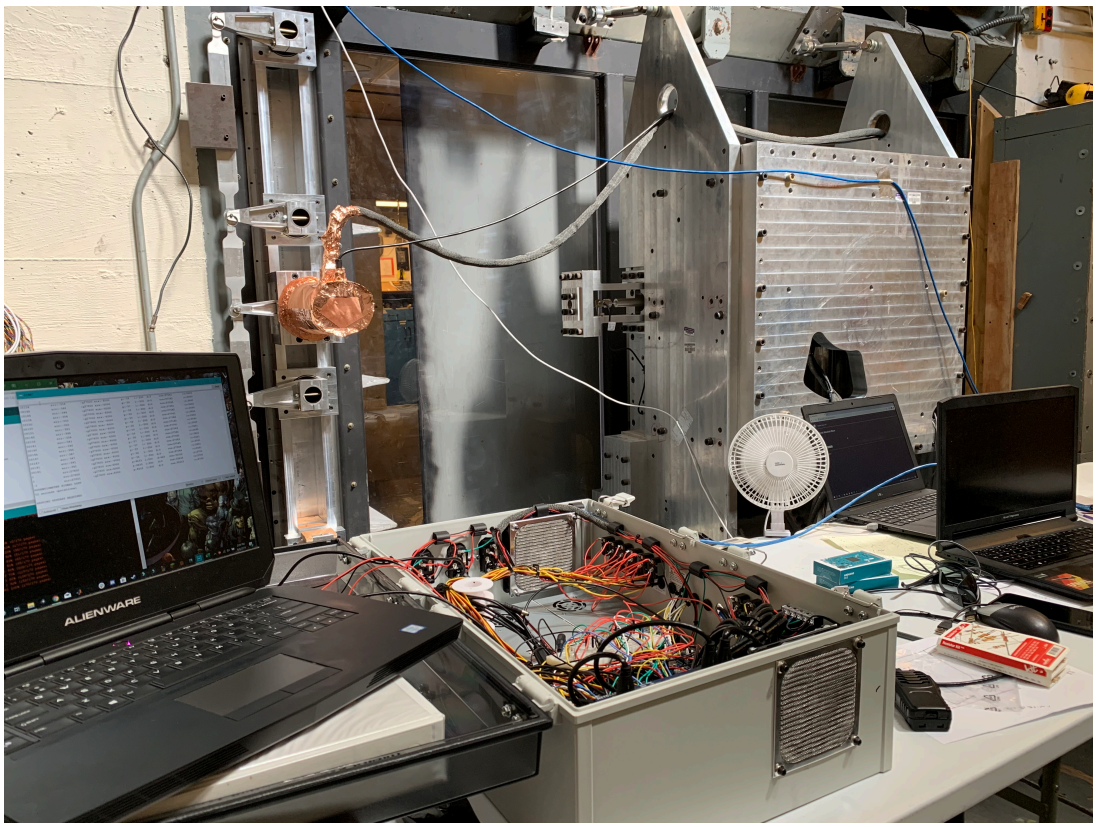

Figure 54: Gust generator, sidewall balance, and control box as seen from Kirsten Wind Tunnel's observation deck

The tunnel also recorded the shape and deformation of the wing in real time using a Vicon Nexus 3D motion tracking system. This system used six Bonita infrared cameras to track reflective markers place on the upper surface of the wing. The software then constructed a skeleton kinematic model that recorded the wing's motion alongside the forces from the sidewall balance during static and wind-on testing. An example of the skeleton used for Wing IV can be seen in Figure 55, and the change in shape from an upward static force at the tip can be seen in Figure 56.

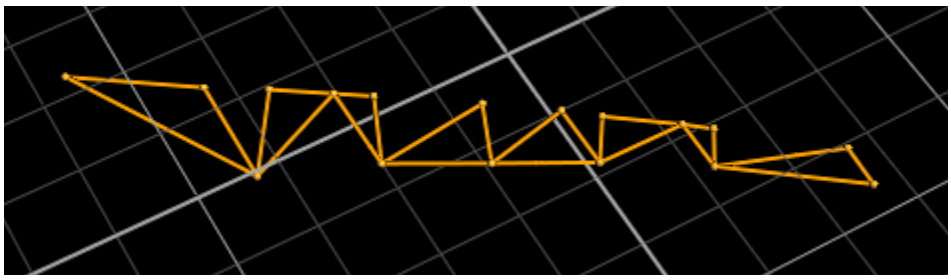

Figure 55: Wing IV Vicon skeleton top view

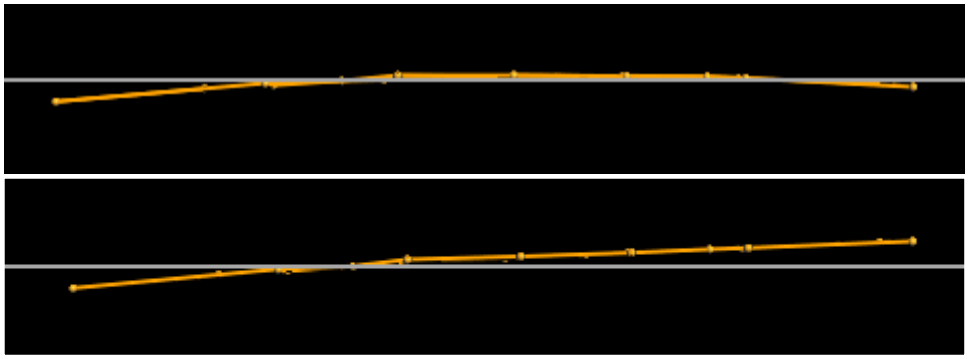

Figure 56: Wing IV Vicon comparison between wind off (top) and static upward load placed at tip (bottom)

12. LESSONS LEARNED

The flap and sensor systems underwent significant troubleshooting to become operational. After correcting simple mistakes, such as shorted wires and floating grounds, pull-up resistors were added to every I^2C bus. On the Dues, pins 20 and 21 (SDA1 and SCL1) were used for communication, which do not have internal pull-up resistors. 2.2 kΩ pull-up resistors were added to both the data and clock lines for each bus in the flap control system near the Arduino. On both lines, 100 Ω resistors were also added in series prior to the signal being read. When combined with the pin capacitance, these series resistors formed a low-pass filter that helped filter out high-frequency noise. In the sensor system, 1.5 kΩ pull-up resistors were added on both the data and clock lines near the accelerometers themselves.

During initial tunnel testing, it was discovered the gust generator motor provided enough electromagnetic interference to shut down the wing's control system when initialized. Once discovered, 100 X 100 copper mesh (McMaster-Carr 9224T87) was wrapped around the large AC motor to act as a Faraday cage, and a shielding wrap-around sleeve (McMaster-Carr 6971T14) was placed around the motor's power wire. Gaps were then sealed with copper foil tape, and the shielding wrap was grounded into the gust generator's control box. This immediately solved the interference issues from the gust generator, and no interference issues have been seen from the gust generator since.

The combination of an Arduino Due and I^2C communication was highly susceptible to noise. After shielding major interference sources like the gust generator, the control system still frequently lost slaves. To combat this, the Arduinos in the control box were removed and separated to have approximately 6 inches of separation between

them. The wires were also redone, with care taken to keep high amperage wires from the communication wires. This helped reduce slave dropouts, but not completely. Within the code, a function was added to send nine clock pulses to the slaves should a failure be detected. The ADCs sent back values between 0 and 32,767 when operating normally, and sent a value of -1 whenever they dropped out. As the data and clock lines were common between the ADC and servo driver, if one was lost, so was the other. When this was read, the clock pulses were sent to all slaves on that I^2C bus. This allowed the wing to revive itself and continue to run even through intermittent dropouts. The drawback of this solution was a delay in any loop of the PID control during which a reset needed to occur. This was typically enough delay (50 msec during a reset versus an approximately 5 msec PID loop) for a flap to drift a degree or two out of position, which would then be corrected once the slaves were reset. The impact of this was reduced by clearing the error terms in the PID whenever a reset occurred.

The servo driver, chosen by SSCI with the intent to increase the resolution of servo commands, failed to operate when more than one bay was operable. After two or three minutes with two bays powered (less if more were on), the servos would no longer be sent PWM commands. The entire system would need to be power cycled to bring back control. This was not a feasible method of operation for testing. Ultimately, this problem with the servo driver was never fixed, but I^2C noise was the suspected culprit. In the end, the servo driver board was removed from the system and the PWM commands were output directly from the digital pins on the Dues. This fixed the problem of control loss, and allowed shakedown testing to commence with closed-loop control. ADC communication still used I^2C, and still exhibited the slave dropout issues mentioned in

the previous paragraph. This problem became worse the more bays that were simultaneously powered.

Further troubleshooting of the I^2C system included wrapping the Dues individually with the copper mesh and tape used to isolate the gust generator. The intent here was to reduce cross talk between the boards themselves, especially after the improvement seen by increasing their spacing. This alteration neither worsened nor improved the system, and was thus removed. In addition, the 3.3 VDC power supply lacked any intentional capacitance. Adding this would serve to clean up and stabilize the power supply to the slaves, preventing brownouts that may have been leading to poor slave operation. 100 μF capacitors were added to the ADC power lines at the ADCs themselves before the servo drivers were removed. No benefit was seen from this addition, but the capacitors were left installed even after servo driver removal.

The dual-material between-flap transition strips, used to smooth the shape at the trailing edge and prevent gaps, were problematic to have printed to the proper size. The initial set ranged from a sixteenth to an eighth of an inch too wide (spanwise). A second set, dimensioned with a smaller width and thinner web to account for this enlargement, also came out too wide, but by approximately half the amount. This was enough to install the transition strips, but induced a buckling along the span of the strips that left a wavy, unclean surface. In both prints, the sidewalls were within tolerance, but the rubber-like filler was not. It was suspected, but unverified, that moisture and heat experienced by the strips during transport and storage caused the filler to stretch. To commence wing testing, the strips were filled with two-part epoxy and allowed to cure. Then, they were split in

half and mounted. This allowed the flaps to be operated and keep a relatively clean surface, but removed the continuous trailing edge aspect from the test.

Two lessons can also be learned from the assembly layup (which led to the requirement for the patching). First, proper support of both the skin and vacuum bag is important to create a clean, crack-free surface with the skins. This was accomplished during the patching layups by placing crudely cut foam blocks into the gaps the vacuum bag could sink into. During the assembly layup, where the skin also covered these gaps, it would have been preferable to use pre-cut, contoured foam pieces that matched the intended OML, and omit from adding resin or epoxy to them so they could be removed after curing was complete. The second lesson would be to plan for manufacturing loads when designing parts. As described in Chapter 5, the rears on some of the bays collapsed along with the skin during the assembly layup. Adding vertical pylons to the part itself, intended to take the load from the compressing vacuum bag, fixed this problem during the patching layups, and should have been implemented prior to the assembly layup. An alternative to this would have been to provide foam supports along the trialing edge, which could have been cut by hand prior to the layup.

13. FUTURE WORK

The design of Wing IV incorporated allowances for additional functionality in future tests. In addition, as some functionality was lost during troubleshooting in order to commence wind tunnel testing faster, full functionality could be restored to the wing.

As mentioned in Chapter 3, double-jointed flaps could be designed and installed in Bays 3 and 4, bringing the total number of independent surfaces to ten. These would use a geometrically scaled copy of the actuation of Bay 2, and the same wiring schematic. The double and single flaps share the same mounting pattern to the ribs, and the mounting points for the servo holders already exist as well.

The cover over Bay 2 was attached with 5/16-18 screws, rather than the 4-40s used on the other bays. These are oversized to allow for the design and mounting of a pylon for an engine or other store to be mounted beneath the wing near the Yehudi break. The bolt layout for the Bay 2 cover, which was simplified to ease pylon design, is shown in Appendix A, along with technical details useful for future design work and repairs of Wing IV.

Nearly every rib has a threaded hole added to its side for the mounting of small weights. These could be used to fine-tune the modes and respective frequencies of the wing. Furthermore, the spar has additional unused space that could be used to mount additional, or a wider variety of, sensors.

During troubleshooting and assembly, the strain gauges in Bays 2 and 4, as well as the accelerometers in Bays 3 through 6, were removed. The strain gauges would repeatedly fall off during the rigors of assembly, and were intentionally left off in order to enter testing faster. New strain gauges, which are in-hand, could be re-bonded, and the

HX711 amplifiers mounted. The strain gauges on the topside of the spar were mounted prior to assembly and the wires are accessible. The accelerometers faced the same setback: a focus on starting testing rather than full functionality. These are also in-hand and could be readily mounted, but would require some additions and modifications to both the wiring and sensor Arduino's code to operate properly.

The initial access covers on Bays 2 through 6 that provide fairings for the actuator protrusions could use improvement. The current covers were made hastily, and while they fulfill their purpose, the edges are not on the same level as the surrounding wing (they did not account for skin, Bondo, and paint thicknesses). Furthermore, the lofting done around the actuators did not focus on aerodynamic efficiency or cleanliness. Finally, some of the thinner areas in the covers could use thickening or reinforcement to help shape retention during testing (little to no effect was seen in static tests with or without covers, so this would be allowable and still flexibility). If additional actuators or sensors were added, or a pylon or similar structural modification was made, some covers would already need to be redesigned to account for these changes.

The CTE (continuous trailing edge) transition strips, as mentioned in Chapter 12, could be redesigned or otherwise reprinted to account for the suspected moisture and heat effects. Conversely, different materials or manufacturer could be chosen (such as those in Wing III) that are not as susceptible to these effects.

Finally, the I^2C communication protocol used to operate the wing needs significant improvement or replacement, as does the control box itself. Dropout of the slave boards was a common problem (namely the ADC), and was ultimately solved with wiring and code alterations. Even so, dropouts continued to be visible in the system, and

while it would recover, it would cause unnecessary delays in control loops. There are numerous options that could be explored to combat this problem, and it is likely a combination of these proposed solutions would provide the best option. First, the pull-up resistors on the data and clock lines could be moved to the farthest point (the ADC in-wing) rather than next to the Arduino, or multiple pairs could be added to these lines for each master/slave. The control box was also very close quarters for all the boards and communication wires. This was altered during testing by removing and spreading out the Dues, then re-wiring the box. This helped reduce dropout frequency, but did not stop the issue from occurring. A new control box, either an additional one or a single box large enough to account for the new spacing, would be beneficial in setting up and troubleshooting future tests. The I^2C wires, especially in the bundle to the wing, could be replaced with twisted-pair wires where each pair is individually shielded, rather than running all the individual wires through the same shielding bundle. A final option would be to replace the I^2C system with a more robust communication protocol, such as CAN, that does not have as much sensitivity to noise as the pairing of a Due and I^2C. This option would require the most time and effort, and increase complexity, but would be worthwhile if shown to improve system reliability.

CONCLUSION

The Wing IV aeroelastic wing model uses a unique blend of composite and traditional wing design to create a highly flexible, yet robust, structure. The actuation system and structure have been demonstrated to have the required strength and meet intended design characteristics. Design, construction, and shakedown testing have been completed of the VCCTEF morphing wing, with initial tests currently underway. Some troubleshooting and improvements are still required to provide optimal functionality of the control and sensing systems. The wing will continue to be available at the University of Washington's Kirsten Wind Tunnel for future testing. Wing IV represents the kind of aeroservoelastic test articles that can produce, in low-speed testing, valuable results in the areas of aeroelastic morphing, VCCTEF, GLA, drag reduction, and real-time control.

BIBLIOGRAPHY

[1] Rajeswari, B., and Prabhu, K.R., "Optimum flap schedules and minimum drag envelopes for combat aircraft", Journal of Aircraft, 1987, Volume 24, Issue 6, pp. 412-414, doi: 10.2514/3.45461

[2] Harris, R., Rickard, W., “Active Control Transport Design Criteria,” Journal of Aircraft, Vol. 16, No. 11, November 1979, doi: 10.2514/3.58598

[3] Holloway, R.B., and Shomber, H.A., the Boeing Company, "Establishing Confidence in CCV/ACT Technology", NTIS Document N76-31162, 1976, https://ntrs.nasa.gov/search.jsp?R=19760024074

[4] Holloway, R.B., Burris, P.M., and Johanenes, R.P., “Aircraft Performance Benefits from Modern Control Systems Technology”, Journal of Aircraft, Vol. 7, No. 6, 1970, pp. 550-553, doi: 10.2514/3.44211

[5] Gilbert, W.W., :”Mission Adaptive Wing System for Tactical Aircraft”, Journal of Aircraft, Volume 18, Issue 7, doi: 10.2514/3.57533

[6] Decamp, R., and Hardy, R., “Mission adaptive wing advanced research concepts”, AIAA Paper 1984-2088, doi: 10.2514/6.1984-2088

[7] Hardy, R., “AFTI/F-111 mission adaptive wing technology demonstration program”, AIAA Paper 1983-1057, doi:10.2514/6.1983-1057

[8] Smith, S.B., and Nelson, D.W., “Determination of the aerodynamic characteristics of the mission adaptive wing”, Journal of Aircraft, Volume 27, Issue 11, doi: 10.2514/3.45965

[9] Renken, J., “Mission-adaptive wing camber control systems for transport aircraft”, AIAA Paper 1985-5006, doi: 10.2514/6.1985-5006

[10] Cosin, R., Angelo, M., Catalano, F., and De Salvi, F.B., “Mission Adaptive Wing Optimization with Wind Tunnel Hardware in the Loop”, AIAA Paper 2010-9201, doi: 10.2514/6.2010-9201

[11] Kota, S., Flick, P., and Collier, F.S., “Flight Testing of FlexFoil Adaptive Compliant Trailing Edge”, AIAA Paper 2016-0036, doi: 10.2514/6.2016-0036

[12] Miller, E.J., Cruz, J., Lung, S.-F., Kota, S., Ervin, G., Lu, K.-J., and Flick, P., "Evaluation of the Hinge Moment and Normal Force Aerodynamic Loads from a Seamless Adaptive Compliant Trailing Edge Flap in Flight", AIAA Paper 2016-0038, doi: 10.2514/6.2016-0038

[13] Weisshaar, T.A., "Morphing Aircraft Systems: Historical Perspectives and Future Challenges", Journal of Aircraft, 2013, Vol.50, pp. 337-353, doi: 10.2514/1.C031456

[14] Valasek, J., "Morphing Aerospace Vehicles and Structures", Wiley, 2012.

[15] Concilio, A., Dimino, I., Lecce, L., and Pecora, R., "Morphing Wing Technologies: Large Commercial Aircraft and Civil Helicopters ", 2018 Elsevier, Ltd.

[16] Vepa, R., "Dynamics of Smart Structures:, Wiley, 2010

[17] Chopra, I., and Sirohi, J., "Smart Structures Technology", Cambridge University Press, 2013

[18] Nguyen, N., and Urnes, J., "Aeroelastic Modeling of Elastically Shaped Aircraft Concept via Wing Shaping Control for Drag Reduction", AIAA Paper 2012-4642, doi: 10.2514/6.2012-4642

[19] Urnes, J., and Nguyen, N., "A Mission Adaptive Variable Camber Flap Control System to Optimize High Lift and Cruise Lift to Drag Ratios of Future N+3 Transport Aircraft", AIAA Paper 2013-214, doi: 10.2514/6.2013-214

[20] Lebofsky, S., Ting, E., Nguyen, N.T., and Trinh, K.V., "Aeroelastic Modeling and Drag Optimization of Flexible Wing Aircraft with Variable Camber Continuous Trailing Edge Flap", AIAA Paper 2013-2443, doi: 10.2514/6.2014-2443

[21] Nguyen, N.T., Ting, E., Nguyen, D.Y., and Trinh, K.V., "Flutter Analysis of Mission-Adaptive Wing with Variable Camber Continuous Trailing Edge Flap", AIAA Paper 2014-0839, doi: 10.2514/6.2014-0839

[22] Kaul, U.K., and Nguyen, N.T., "Drag Optimization Study of Variable Camber Continuous Trailing Edge Flap (VCCTEF) Using OVERFLOW", Paper AIAA 2014-2444, doi: 10.2514/6.2014-2444

[23] Nguyen, N.T., Livne, E., Precup, N., Urnes, J., Nelson, C., Ting, E., and Lebofsky, S., "Experimental Investigation of a Flexible Wing with a Variable Camber Continuous Trailing Edge Flap Design", AIAA Paper 2014-2441, doi: 10.2514/6.2014-2441

[24] Morris, C., Sheahan, J., Dykman, J., Clingman, D., and Urnes, J., "Control System Design for a Variable Camber Continuous Trailing Edge Flap System on an Elastic Wing", AIAA Paper 2014-0835, doi: 10.2514/6.2014-0835

[25] Ting, E., Dao, T., and Nguyen, N.T., "Aerodynamic Load Analysis of a Variable Camber Continuous Trailing Edge Flap System on a Flexible Wing Aircraft", AIAA Paper 2015-1839, doi: 10.2514/6.2015-1839

[26] Nguyen, N.T., Ting, E., and Lebofsky, S., "Aeroelastic Analysis of Wind Tunnel Test Data of a Flexible Wing with a Variable Camber Continuous Trailing Edge Flap (VCCTEF)", AIAA Paper 2015-1405, doi: 10.2514/6.2015-1405

[27] Lebofsky, S., Ting, E., and Nguyen, N.T., "Multidisciplinary Drag Optimization of Reduced Stiffness Flexible Wing Aircraft with Variable Camber Continuous Trailing Edge Flap", AIAA Paper 2015-1408, doi: 10.2514/6.2015-1408

[28] Boskovic, J., Wise, R., Jackson, J.A., and Nguyen, N.T., "A Flutter Suppression and Drag Optimization Approach for Flexible Aircraft", AIAA Paper 2017-1588, doi: 10.2514/6.2017-1588

[29] Ting, E., Chaparro, D., and Nguyen, N.T., "Aero-Structural Optimization of Variable Camber Continuous Trailing Edge Flap Configurations Using Transonic and Viscous Potential Flow Method", AIAA Paper 2017-4220, doi: 10.2514/6.2017-4220

[30] Kaul, U.K., and Nguyen, N., "Extending A Correction Method for Unsteady Transonic Aerodynamics to Variable Camber Continuous Trailing Edge Flap", AIAA Paper 2019-3157, doi: 10.2514/6.2019-3157

[31] Precup, N., Mor, M., and Livne, E., “Design, Construction, and Tests of an Aeroelastic Wind Tunnel Model of a Variable Camber Continuous Trailing Edge Flap (VCCTEF) Concept Wing”, AIAA Paper 2014-2442, doi: 10.2514/6.2014-2442

[32] Precup, N., Mor, M., and Livne, E., "The design, construction, and tests of a concept aeroelastic wind tunnel model of a high-lift variable camber continuous trailing edge flap (HL-VCCTEF) wing configuration", AIAA 2015-1406, doi: 10.2514/6.2015-1406

[33] Nguyen, N., Precup, N., Livne, E., Urnes, J.M., Dickey, E., Nelson, C, Chiew, J., Rodriguez, D.L., Ting, E., and Lebofsky, S., "Wind Tunnel Investigation of a Flexible Wing High-Lift Configuration with a Variable Camber Continuous Trailing Edge Flap Design", AIAA Paper, 2015-2417, doi: 10.2514/6.2015-2417

[34] Espana, M., and Gilyard, G., "Direct Adaptive Performance Optimization of Subsonic Transports: A Periodic Perturbation Technique", NASA TM-4676, March 1995.

[35] Brown, N., "Peak-Seeking Control for Reduced Fuel Consumption: Flight-Test Results for the Full-Scale Advanced Systems Testebed F/A-18 Airplane", August 2013, https://ntrs.nasa.gov/archive/nasa/casi.ntrs.nasa.gov/20140008929.pdf

[36] Brown, N.A., and Schaefer, J.R., "Peak-Seeking Optimization of Trim for Reduced Fuel Consumption: Flight-Test Results", AIAA Paper 2013-5171, doi: 10.2514/6.2013-5171

[37] Schaefer, J.R., and Brown, N.A., "Peak-Seeking Optimization of Trim for Reduced Fuel Consumption: Architecture and Performance Predictions", AIAA Paper 2013-4856, doi: 10.2514/6.2013-4856

[38] CRM - https://commonresearchmodel.larc.nasa.gov/)

[39] Vassberg, J.C., DeHaan, M.A., Rivers, M.S., and Wahls, R.A., "Retrospective on the Common Research Model for Computational Fluid Dynamics Validation Studies", Journal of Aircraft, 2018, July-August, Volume 55, Issue 4, pp. 1325-1337, doi: 10.2514/1.C034906

[40] Precup, N., Mundt, T. Mor, M., and Livne, E., "An Active Variable Camber Continuous Trailing Edge Flapped Wing Wind Tunnel Model for Aeroelastic "In-Flight" Shape Optimization Tests", AIAA Paper 2018-3106, doi: 10.2514/6.2018-3106

[41] Nguyen, N.T., Cramer, N.B., Hashemi, K.E., Ting, E., Drew, M., Wise, R., Boskovic, J., Precup, N., Mundt, T., and Livne, E., "Real-Time Adaptive Drag Minimization Wind Tunnel Investigation of a Flexible Wing with Variable Camber Continuous Trailing Edge Flap System", AIAA Paper 2019-3156, doi: 10.2514/6.2019-3156

[42] Precup, N., "Design and Construction of a Wind Tunnel Model with Active Variable Camber Continuous Trailing Edge Flap for Aeroelastic “In-Flight” Shape Optimization Tests", MSAA Thesis, 2018, William E. Boeing Department of Aeronautics and Astronautics, University of Washington, Seattle

APPENDIX A

Mechanical Details for Repairs and Further Work

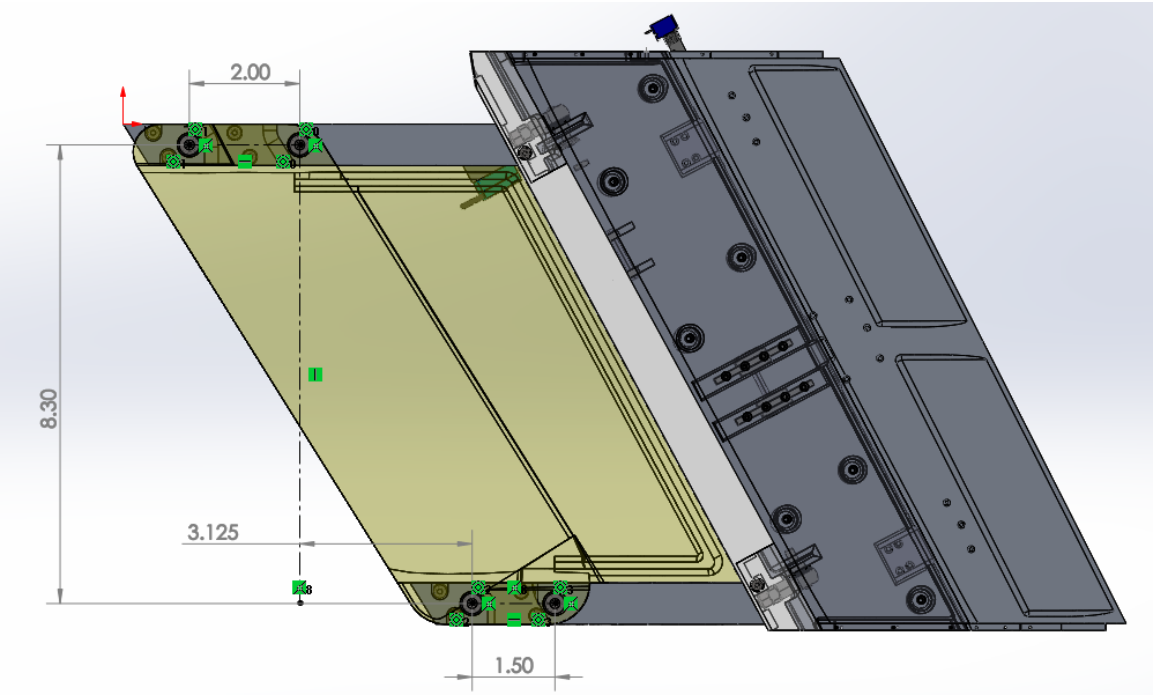

Figure 57: Flap 2 cover simplified mounting layout for pylon mounting

Table 9: Thread Size Overview

Area / Part	Thread size
Adapter to Sidewall	3/8-16
Adapter to Wing	1/2-13
Root Cover	6-32
Flap 1, 3-6 Covers	4-40
Flap 2 Cover	5/16-18
Servo to Mount	8-32
Servo Mount to Spar	8-32
Servo Horn to Servo	M3 X 0.5
Servo Horn to Control Rod	1/8” Dia. Shoulder 4-40
Control Rod	6-32
C-Rears to Ribs	4-40
Flap 2 Rear Winglets	6-32
Inter-Tip Mounting	2-56
Tip Weight Mounting	2-56
Tip Core to Spar	6-32
Transition Strip Mounting	0-80
RBLD4 to Ribs & Flap	M4 X 0.7
Single Flap Inter-Mounts	2-56
Sensor Mounts to Spar	4-40
Flap 2 ADC Mount to Rib	8-32
HX711 to Mount	4-40
ADC to Mount	2-56
Accelerometer to Mount	4-40
String Potentiometer Mounting	2-56
Linear Rail Mounting	M1.6 X 0.35
Linear Rail Carriage Mounting	M2 X 0.4
Flap 1A Internal	2-56
Flap 1B Internal	1-72
Flap 2A Internal	2-64
Flap 2B Internal	1-72

Table 10: Manufacturer and Supplier List

Part(s)	Manufacturer / Supplier
Load Block Flap 1 Well Spar	Protocase
Root Plates Servo Mounts Spar Brackets Wing Adapter	Momentum Manufacturing and Prototype
Foam	AeroTEC
Fiberglass Skin	Fiberlay
Layup Consumables	Fibre Glast Developments Corp.
Fiberglass Film	Pacific Coast Composites
3D Printed Transition Strips	FATHOM
3D Printed Rears 3D Printed Covers 3D Printed Sensor Trays	Proto Labs, Inc.
Flaps Ribs Tip	3D Hubs
Servo Horn	ServoCity
Servos	AJ Aircraft
RBLD4 (for Flap Mounting)	MISUMI Corporation
Fasteners Rod Ends Tools Epoxy Control Box and Hardware	McMaster-Carr
String Potentiometers	UniMeasure, Inc.
Bourns Potentiometers	Digi-Key Electronics
HX711 Load Cell Amplifier Multiplexer Electronics Consumables	SparkFun Electronics
Arduino Dues Ethernet Shields	Arduino
Wires	Amazon.com, Inc.
ADCs Servo Drivers Electronics Consumables	Adafruit Industries
Servo Power Supplies	Allied Electronics & Automation
Accelerometers	Analog Devices, Inc.
Strain Gauges	OMEGA Engineering